National Physical Laboratory

NPL REPORT MAT 119

TENSILE PROPERTY MEASUREMENT OF LATTICE STRUCTURES

A T FRY, L E CROCKER, M J LODEIRO, M POOLE, P WOOLLIAMS, A KOKO, N LEUNG[1], D ENGLAND[1], C BREHENY[2]

MARCH 2023

[1] University of Surrey
[2] HiETA Technologies

TENSILE PROPERTY MEASUREMENT OF LATTICE STRUCTURES

A T FRY, L E CROCKER, M J LODEIRO, M POOLE, P WOOLLIAMS, A KOKO, N LEUNG[1], D ENGLAND[1], C BREHENY[2]

Advanced Engineered Materials
[1]University of Surrey
[2]HiETA Technologies

ISSN 1754-2979

DOI ADDRESS: https://doi.org/10.47120/npl.MAT119

National Physical Laboratory
Hampton Road, Teddington, Middlesex, TW11 0LW

This work was funded by the UK Government's Department for Science, Innovation & Technology through the UK's National Measurement System programmes.

Approved on behalf of NPLML by
Stefanos Giannis, Science Area Leader.

CONTENTS

1 INTRODUCTION 1
2 SPECIMEN DESIGN AND MANUFACTURE 3
3 MECHANICAL TESTING 10
3.1 SINGLE LIGAMENT 10
3.1.1 Universal Test System 10
3.1.2 Universal Test System Results 12
3.1.3 In-situ Micro Test System 17
3.1.4 In-situ Micro Test System Results 19
3.2 LATTICE UNIT CELL 23
4 FINITE ELEMENT MODELLING 27
4.1 SINGLE LIGAMENT MODEL 27
4.2 LATTICE MODEL 30
5 DISCUSSION 39
6 CONCLUSIONS 43
7 REFERENCES 44

1 INTRODUCTION

Additive manufacturing (AM) has enabled designers and engineers to produce increasingly complex geometries and components. Selective laser melting (SLM) manufacturing has been particularly instrumental in this. Through careful control of the processing parameters and build angles and supports structures, manufacturers can now realise their theoretical design concepts more readily and produce complex structures such as lattices. Lattice structures have the capacity to generate unique mechanical, electrical, thermal and acoustic properties[1]. There has been a large amount of information published relating to the mechanical properties of these structures. Generally, the mechanical testing of SLM lattices has been performed under compression [2,3,4]. This form of testing for lattices is relatively more straightforward to carry out and analyse than tensile testing. The compression test can be simply performed by compressing an as-manufactured lattice between two platens. When testing in tension there are more challenges to overcome, for example how to attach the lattice structure to the testing apparatus. It has been reported that this area of the test piece is critically important, and that this region can be responsible for premature failure due to stress concentrations at the interface[5]. In the work by Alsalla *et al*, six samples, manufactured both parallel and perpendicular to the build direction, were pulled under uniaxial tension using an EZ20 universal material testing machine (Lloyd Instruments Ltd., UK) at a constant rate of displacement of 0.5 mm/min. The stress-strain curves of the tensile tests on the gyroid cellular lattice structures are shown in Figure 1. It was found that all of the samples fractured close to the solid end plate where the struts join the non-cellular end tabs required to introduce the tensile load, as seen in X-ray computed tomography (X-ray CT) images in Figure 2: e. This was attributed to the sudden change in density and, thus stiffness, forming a local stress concentration. Comparing to the deformation at the centre of the sample, in Figure 2: b, clearly shows how the end constraints locally affect the deformation of the cellular solid, and that the centre section is clearly not dominated by the constraint at the sample ends.

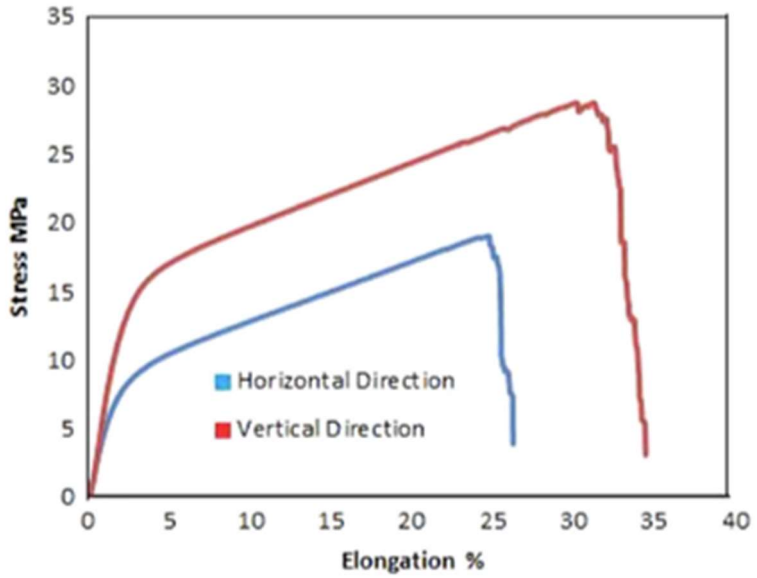

Figure 1 Stress-strain curves of the tensile tests on the cellular lattice structures from Alsalla *et al* [5]

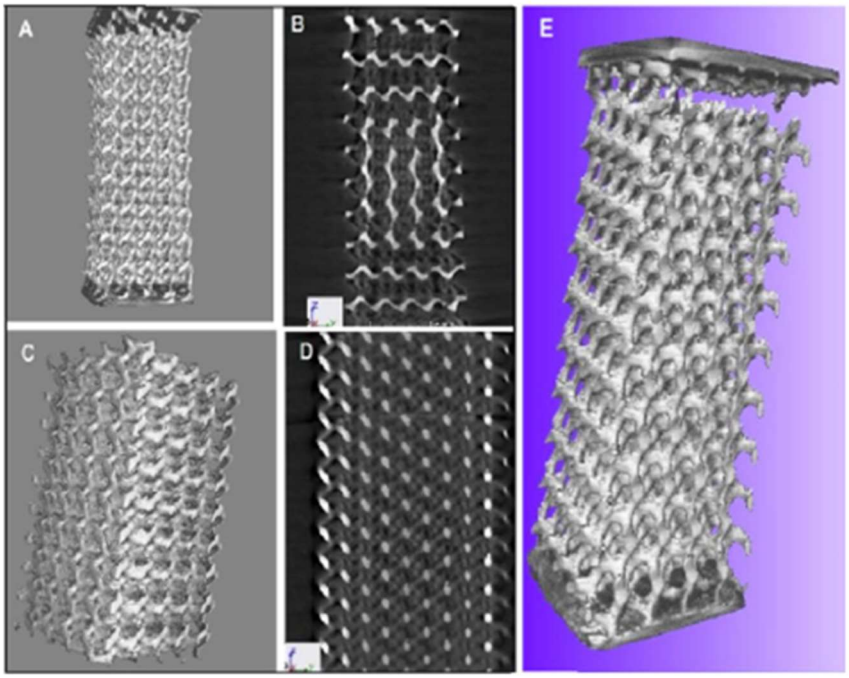

Figure 2 X-ray CT scans of the cellular lattice structure before and after a tensile test. (A) and (E) show the sample after testing with the detail of the rupture clearer in (E). (B) is a 2D slice through the sample after rupture showing rotation of internal struts. (C) and (D) show the sample before testing, with B showing the internal struts in the initial unrotated configuration[5]

As is the case in any component manufactured by SLM, the final material properties are highly dependent on the processing parameters used during manufacture [6]. For the purposes of this work, the processing conditions were kept the same for each build. Since the emphasis of this work is on the development and validation of a measurement method for evaluating the tensile properties of lattice structures, this build consistency is highly appropriate. There has been research on the optimisation of processing parameters to obtain comparable material properties between SLM AlSi10Mg and conventionally cast AlSi10Mg. Kempen *et al* [7] identified SLM process parameters for AlSi10Mg that obtain mechanical properties comparable to cast materials: E = 68 GPa, UTS = 396 MPa, HV = 127.

Aside from the processing parameters, many physical parameters have been reported which also affect the properties of lattices; these include powder morphology, size and chemical composition [8], as well as particle size distribution [9], laser exposure strategy and power, laser scan speed, and layer thickness. This is discussed further by Maconachie *et al* [1]. The mechanical properties of lattice structures, in particular compressive strength and modulus, are dependent on factors such as: cell geometry; structural boundary and loading conditions; as well as the relative density (ρ/ρ_s) of the lattice density (ρ) to the solid material density (ρ_s)[10]. Leary *et al* [11] state that the mechanical properties are particularly influenced by whether the cell geometry results in a loading response of the lattice struts that is either stretch-dominated or bending-dominated. Such considerations are once again beyond the scope of this work and report, the reader is referred to Leary *et al* [11] for more information.

Analytical models to predict the mechanical behaviour of cellular structures can be found dating as far back as the 1950s but, with the modern adoption of Finite Element (FE) methods, various numerical models for predicting this same response have recently been developed. Much work has been conducted to determine the influence and effects of microstructural and manufacturing defects on the accuracy of FE models. Once again inclusion of such information at this stage is beyond the scope of this work but the reader is directed to the short review by

Maconachie *et al* [1]. One of the conclusions of this review is that the tensile performance of SLM lattice structures is still not well defined as most research uses compressive experiments for identification of their mechanical properties, largely due to the greater difficulty of tensile lattice experimental design [1]. The development of a simple and repeatable approach to measuring the tensile properties of lattices is the first step to achieving this.

2 SPECIMEN DESIGN AND MANUFACTURE

There are several different design approaches taken in the literature to facilitate tensile testing of lattices. These have tended to focus on quite large multi-cellular lattices as illustrated in Figure 3. The specimens have a cross-sectional area of 4 x 4 cells (around 10 x 10 mm) with four cells in height that have constant density at the lattice centre and two layers of cells either side closest to the grips with graded density, in order to smooth the transition between the lattice and the grips and to localize failure in the central region. A graded density was obtained by linearly increasing the struts diameter, from 0.6 to 0.8 mm in the layer closest to the lattice centre and from 0.8 to 1.2 mm in the next layer, closest to the grips [12]. Other examples of this approach and specimen design are shown in Figure 4 to Figure 6. These all focus on quite large lattice elements and structures. The aim of the work presented here was to focus on individual elements of the lattice and scale this up to larger lattice structures, hence a different approach to the specimen design was needed.

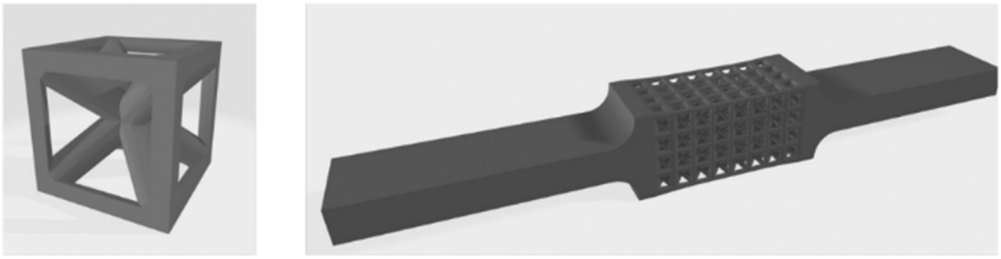

Figure 3 SC-BCC unit cell (A) and specimen geometry (B) with graded density to smooth transition between lattice and grips, used for monotonic tension and compression tests [12]

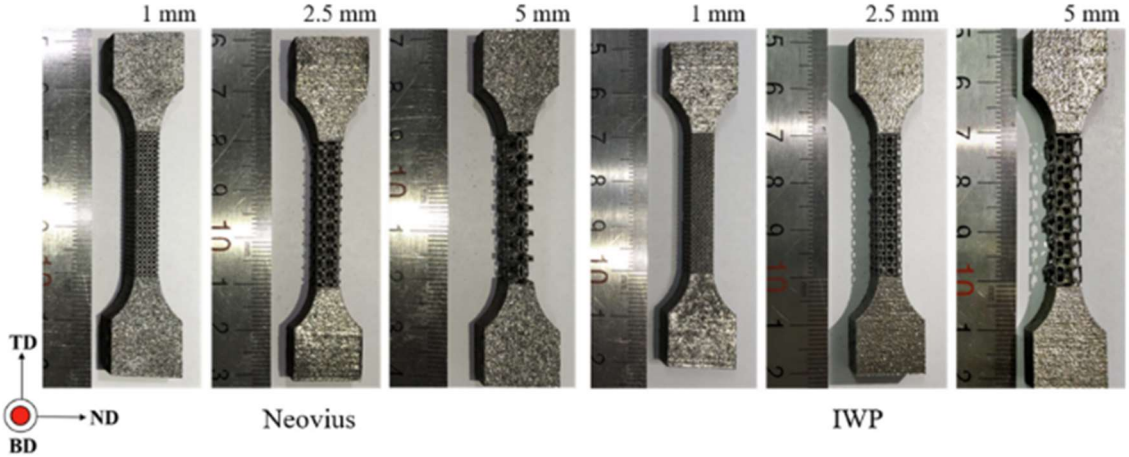

Figure 4 Macrophotographs of Co-Cr-Mo TPMS sheet lattice specimens with various topology and unit cell sizes: Neovius (left) and IWP (right). The legend on the left shows the directions of the three axes in the Cartesian coordinate system (BD: building direction, TD: tensile test direction, ND: Normal direction) [13]

Figure 5 Macroscopic appearance of broken tensile samples [14]

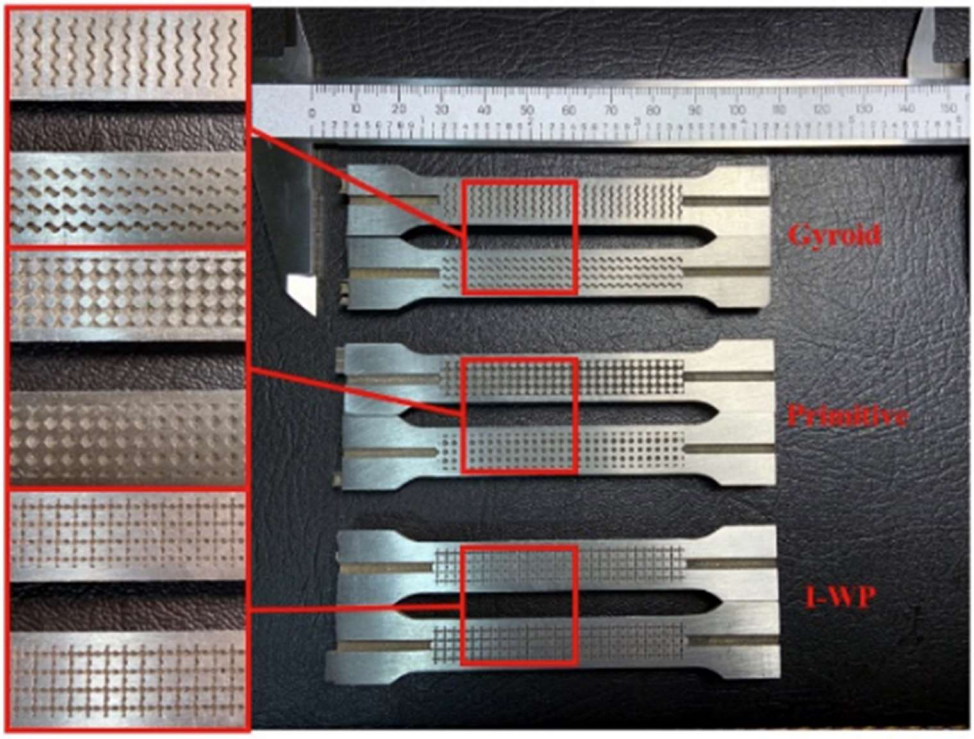

Figure 6 The porous test specimens manufactured by SLM [15]

It was important, in order to be able to realise this work, that the specimen design could be tested in a range of equipment and did not require specially developed mounts or grip systems. There was a conscious decision therefore to ensure that the sample could be both gripped in wedge action grips which are commonly found on universal test systems and could also be gripped with a simple plate system secured using bolts, a system commonly found in apparatus for small scale sample testing. The design took inspiration from an approach used in single fibre testing where the fibre is usually supported by some form of framing support material that

can be disconnected from the load chain after gripping the specimen but before full test loading, thus preventing premature failure of the fragile samples during the gripping stage.

There were two specimen forms that were of interest in this work. The first was the lattice struts or ligaments which form the long axis of the lattice unit cells connected by nodal points. The second form was the lattice unit cell itself, consisting of a minimal number of lattice cells within this phase of the work.

Ligament design was performed in the opensource parametric CAD program OpenSCAD, to enable the designs to be generated with different design parameters rapidly and simply. The generated CAD design was saved as a surface tessellation model (STL) file for printing. Care was taken to ensure that sufficient detail was generated so that the smooth curves of the small gauge sections and tapers was faithfully reproduced, see Figure 7.

The sample was made by combining the required cylindrical gauge length to two rectangular grip sections (1 mm thick, 10 mm wide and at least 20 mm long) and then blending the gauge into the grip sections to give a smooth transition. This was achieved by subtracting a torus that touched the top of the gauge section (its inner diameter was the same as the gauge section outer diameter) and that had an 8 mm tube diameter (to set the length of the taper region) shown in Figure 8. Thus, the maximum gauge thickness that could be smoothly transitioned was the same as the grip thickness (1 mm) but would seamlessly handle gauge diameters that were much less than the grip thickness, see Figure 9.

The gripping portion of the test pieces extended to a sufficient length to ensure adequate gripping area for a variety of gripping solutions and test systems. The grip section also provides the end user with the ability to include markers to identify the samples. In the example shown in Figure 10, indents have been manufactured in the top and bottom end tabs (in this case two hemispheres on the left- and right-hand side of the top and bottom end tabs). IDs can also be manufactured onto the end of the specimen if necessary. This is shown in Figure 11 which shows a single manufacture test piece with four ID dots manufactured into the top and bottom end tab.

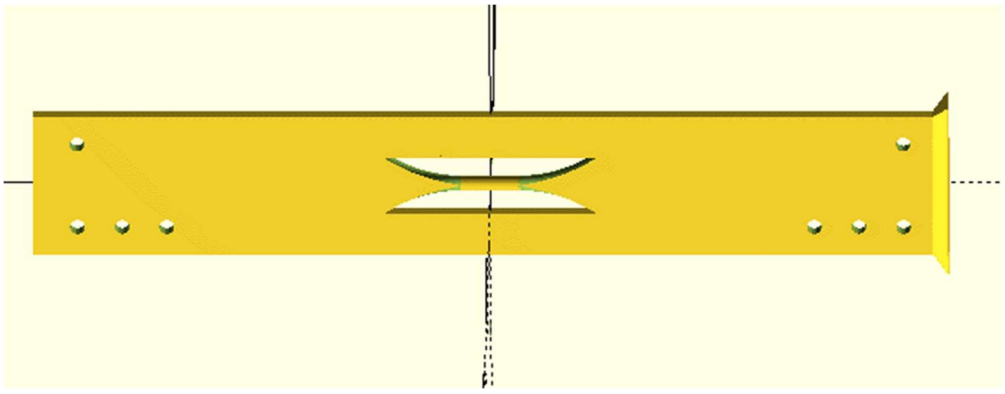

Figure 7 Single ligament design

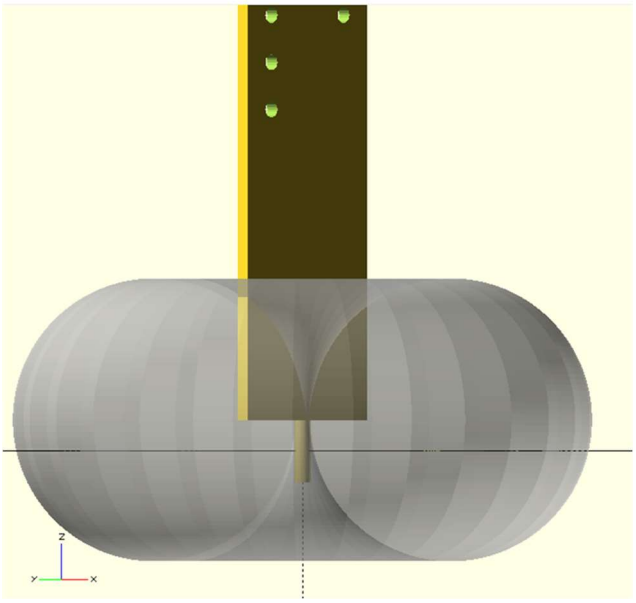

Figure 8 Torus subtraction from gauge-and-grip shape

Figure 9 Example of resulting taper

To either side of the ligament piece are two thick supporting bars, each 3 mm wide, which bridge across the top and bottom half of the test piece. These provide strength and support to the top half of the test piece and to protect the ligament during manufacture and powder removal, as well as protection from any applied load during the mounting of the test piece into the universal test machine prior to testing. Once in position the side supports can be simply but carefully cut through with a grinding tool (such as a Dremel ®) or with a fine hacksaw.

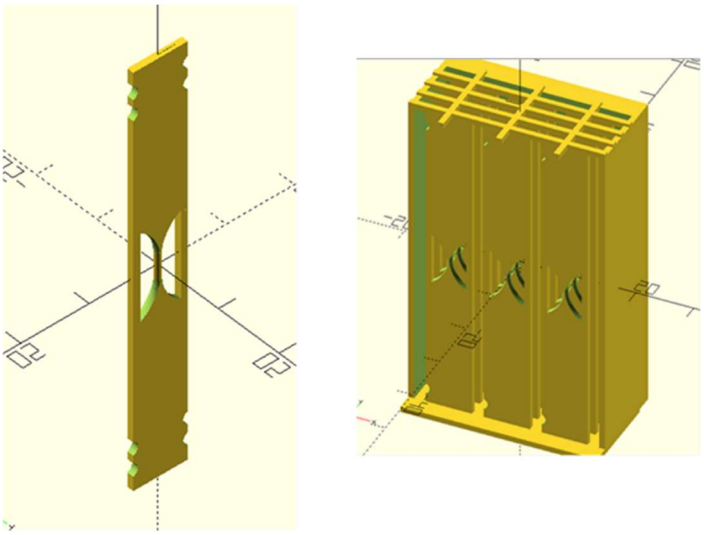

Figure 10 Design of single ligament test specimen and multiple specimen cassette

To further protect the test piece during manufacture, handling and transport, a cassette design was used to allow numerous samples to be manufactured and held together in a spur-type configuration. This is shown on the right-hand side of Figure 10. The test pieces are manufactured in a grid and then encased on all four sides by a solid wall of material locally punctuated with holes for post-manufacture processes. A 2D x-ray image of the as-manufactured cassette encased test pieces is shown in Figure 12. This also illustrates how the dots can be used to uniquely identify the test pieces, in Figure 12 test pieces 3, 7, 6 and 8 are shown from left to right.

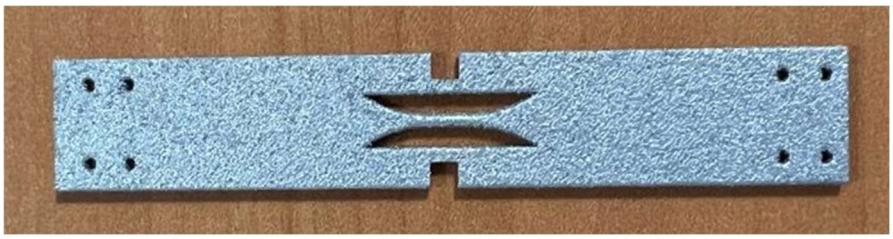

Figure 11 Single ligament test specimen manufactured from AlSi10Mg

For the work reported here, four test pieces were arranged together for each of four gauge lengths equalling 1, 2, 3 and 4 multiples of the constant gauge (ligament) diameter of 1 mm providing 16 samples in total, Figure 13. In order to efficiently pack these together into a single build cassette, the maximum sample length was found (in this case for the samples with gauge length equivalent to 4 times the gauge diameter) and the grip sections for the 1, 2 and 3 times samples were made commensurately longer so all the samples had the same overall length. Chamfers were added to the top and bottom to aid building.

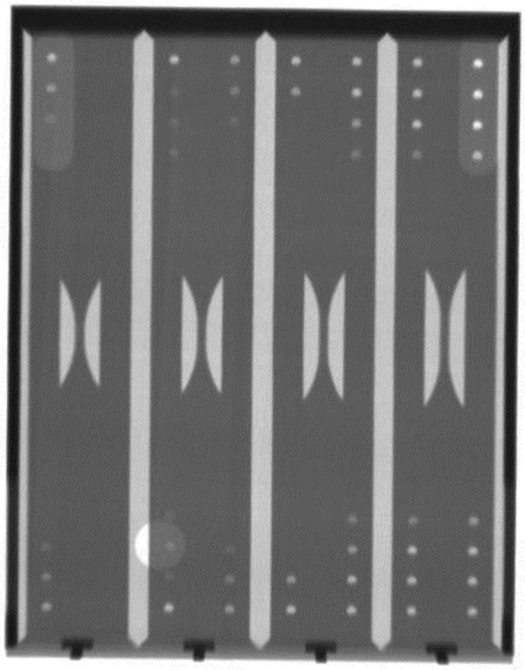

Figure 12 X-ray image of four stacks of single ligament test specimens in the multi-specimen cassette (Note other layers lie behind those seen in the image)

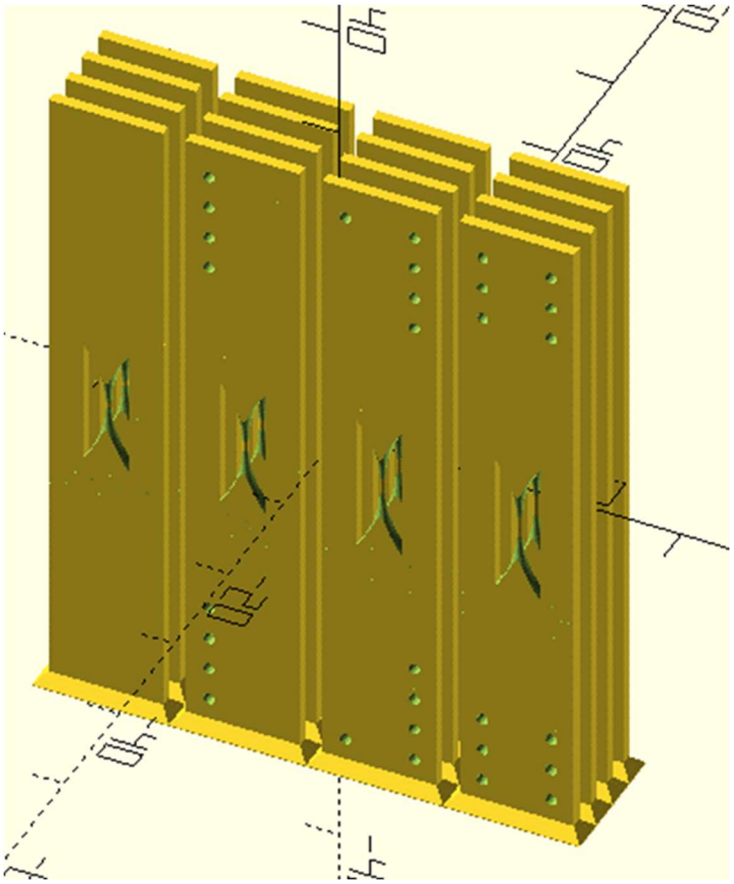

Figure 13 Example of 16 samples arranged together

Finally, a solid base was added and a thin 1 mm thick wall surrounded all the samples, with holes through the side to allow powder removal and identification of the block. The external holes were positioned away from the centre so that the gauge sections were protected from accidental damage. The sample tops were connected by a thin grid to stop accidental deformation during handling. Examples of the actual cassettes can be seen in Figure 14 showing examples of cassette builds at different angles to the build plate with corresponding support structure. The samples were made either vertically or with an additional angled base block so that the samples were built with an angle of 35.6° from the horizontal.

Figure 14 Example of cassette design showing the holes in the side walls for powder removal purposes

Having developed a test piece design and manufacturing approach, the design could be extended for use with lattice cells, as shown in Figure 15. This shows a single line consisting of nine lattice cells attached to grip sections, keeping consistent with the single ligament sample. As before the main test piece is protected from accidental or premature damage by side supports.

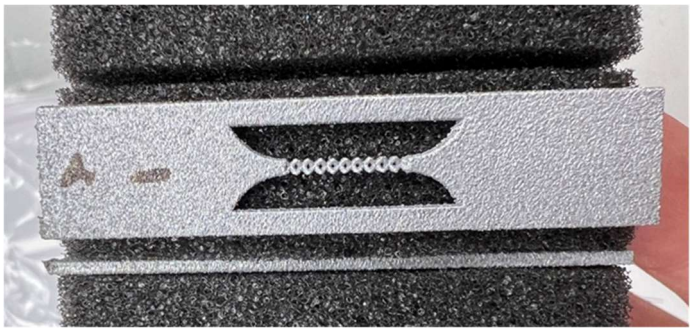

Figure 15 Example of a lattice test piece

All test pieces were manufactured from AlSi10Mg powder using a laser powder bed manufacturing route on a Renishaw 500Q.

3 MECHANICAL TESTING

3.1 SINGLE LIGAMENT

3.1.1 Universal Test System

Tensile tests were conducted using an Instron 5969 universal mechanical test machine fitted with a 50 kN load cell. The coupons were gripped using a pair of wedge action grips fitted with serrated grip faces. The alignment of the test machine and grips was set prior to testing the ligaments by gripping a stiff steel bar and loading to 1 kN before firmly locking the position of the grips. The test pieces were loaded for initial tests at a crosshead speed of 1 mm per minute until failure.

Prior to testing, the test pieces were speckled using white and black spray paints. Strain was subsequently measured on opposing faces of the test piece using a non-contact video extensometer (Imetrum ®). The test setup is illustrated in Figure 16, showing the test piece gripped in the wedge action grips and the two cameras imaging the front and back face of the test piece for non-contact strain measurement. A closer view of the test piece in the grips is given in Figure 17.

The non-contact strain measurement method allows strain to be measured in several different ways from a single dataset. The user can use a full field approach and measure the strain over the whole gauge length, or multiple discrete areas can be selected allowing the user to simulate a standard strain gauge measurement, or markers can be used combined with a video extensometer approach can be employed. An example of the images captured is shown in Figure 18.

Figure 16 Instron universal test machine setup used for testing with cameras imaging front and back faces of the test piece simultaneously for strain measurement

Figure 17 Single ligament test piece held in wedge action grips

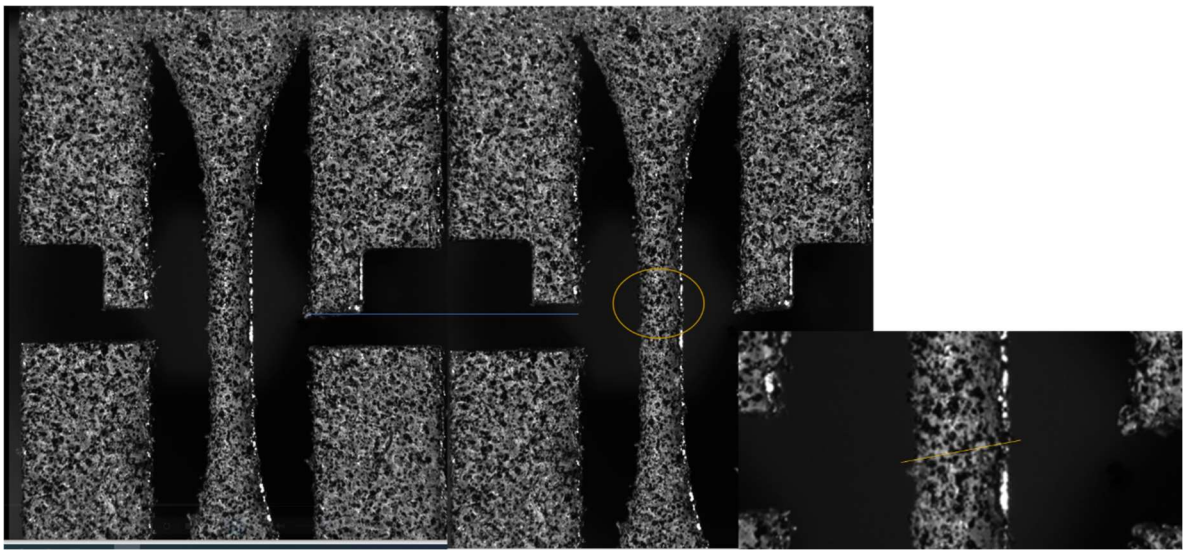

Figure 18 Captured frames from the Imetrum video of a test showing the initial frame (far left) final frame (middle) and a closeup of the failure in the final frame with the fracture marked by the yellow line (far right)

3.1.2 Universal Test System Results

The results of the tests on the 1 mm diameter ligament sample with a gauge length of 2, 3 and 4 mm are presented in Figure 19. The stress has been calculated using an assumed diameter of 1 mm, this is a nominal value as the material was tested in the as-manufactured condition and so some surface roughness will be present. This can be seen in Figure 20 which shows one of the ligament test pieces imaged in the Starrett MVR 300 optical measurement system. This image also shows the speckle pattern on the test piece. From Figure 20 it can be seen that there are surface asperities on the gauge length. Measured optically, the minimum diameter was found to be 1.070 mm, the maximum value was 1.081 mm and the mean value was found to be 1.076 mm. The plot of stress against strain is shown in Figure 21. This shows that repeatability between the three measured samples is very good. Further repeat measurements were conducted on the single ligament test pieces to determine the degree of variability in the material properties and the effect of test rate, reduced in these instances to 0.1 mm/min, presented in Figure 22. Whilst there is some scatter in the load-displacement curves, when the data is plotted as stress against strain the curves converge, as shown in Figure 23. Apart from one outlier (2AJIN002) the rest of the repeat measurements follow the same curve up to the yield point, after which they start to diverge and finally fail at elongations of 11% to 24.5% average strain. Note that the strain is reported in Figure 23 as an average because the front and rear face of the sample was observed with the Imetrum ® non-contact strain system, and it is the average of these two values that has been used. The two-sided imaging enables bending in the test piece to be monitored, which can often help to explain unexpected scatter in the results.

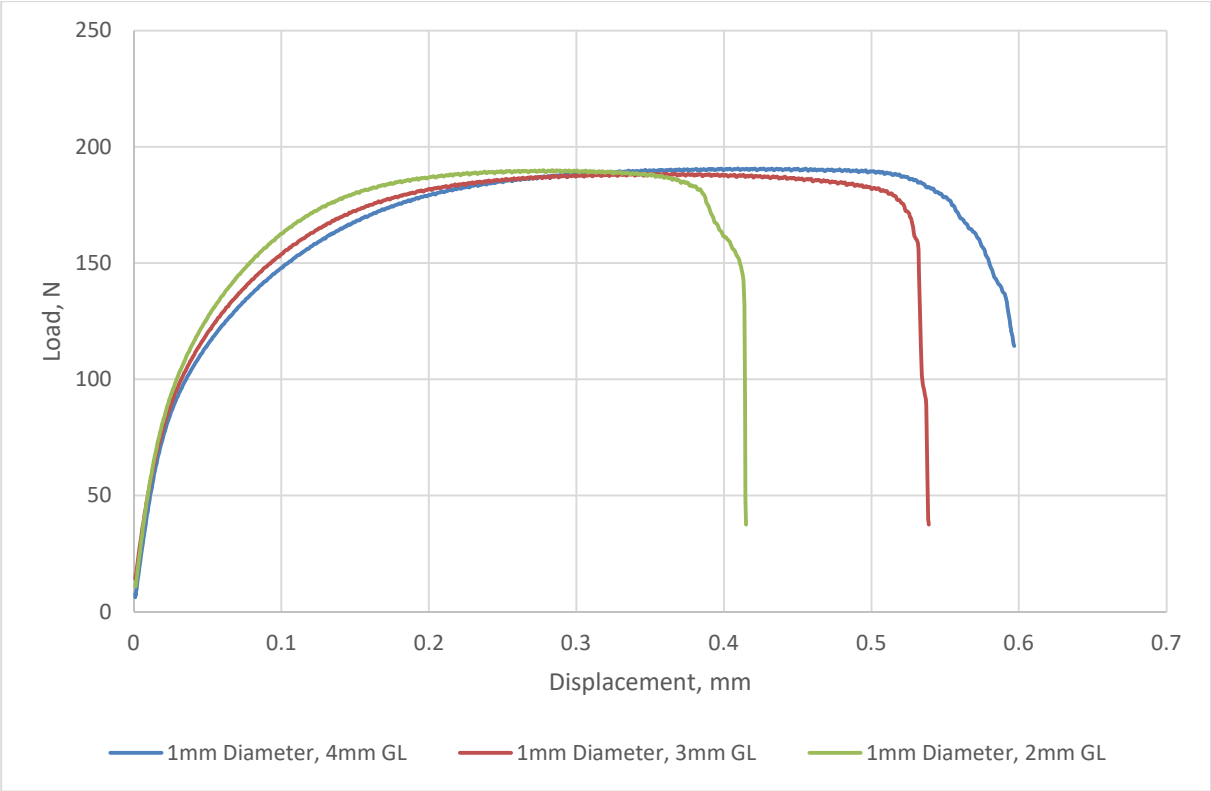

Figure 19 Load vs displacement results for the 1mm diameter single ligament samples

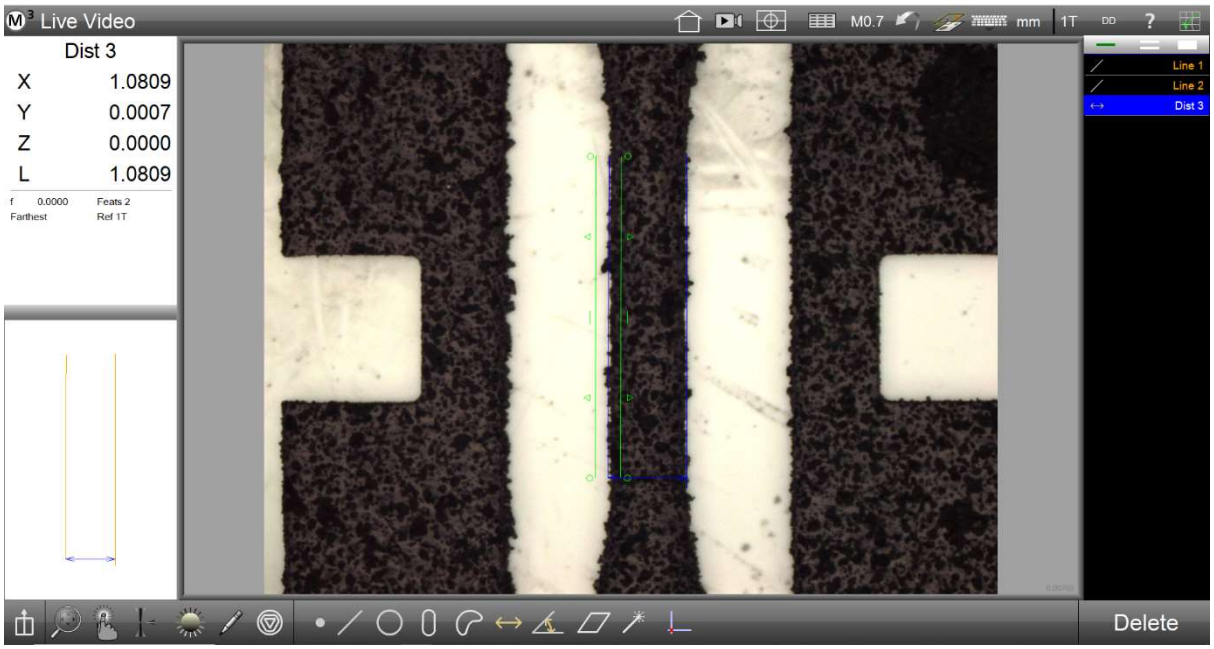

Figure 20 Image from the Starrett MVR 300 optical measurement system

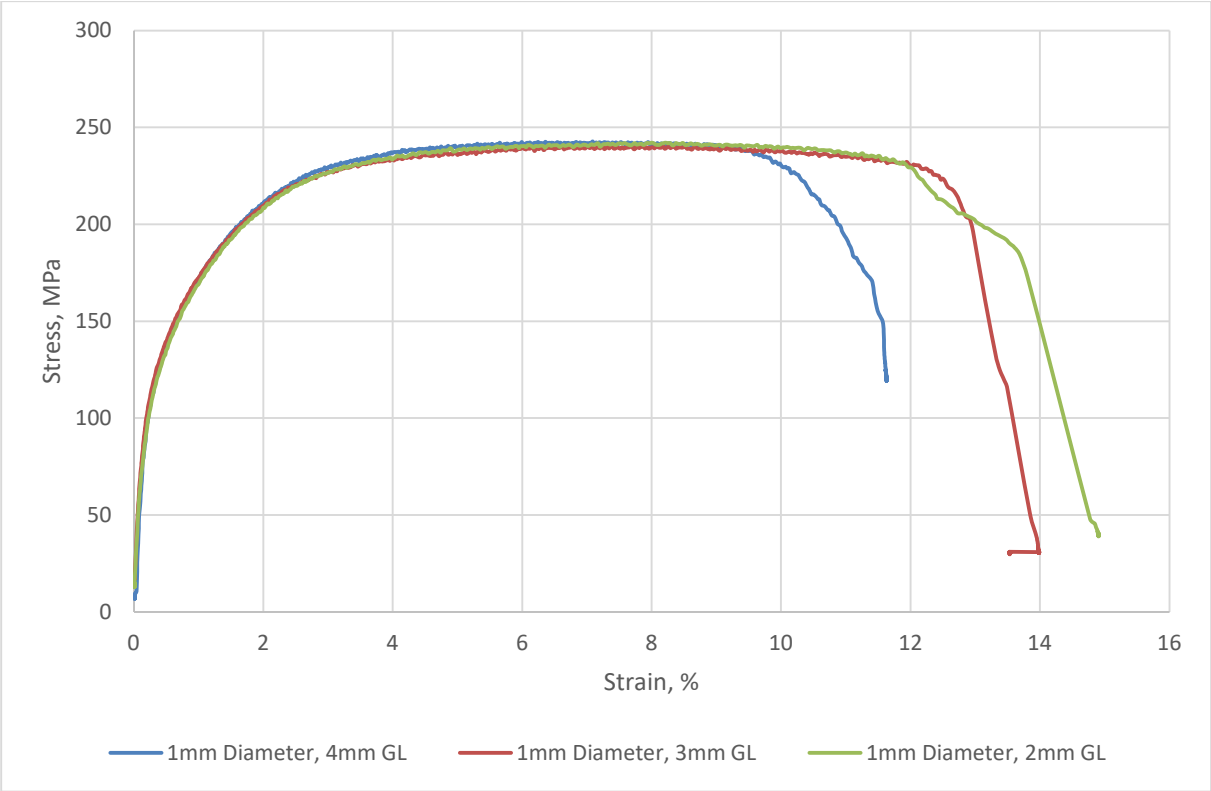

Figure 21 Stress vs strain results for the 1 mm diameter single ligament samples

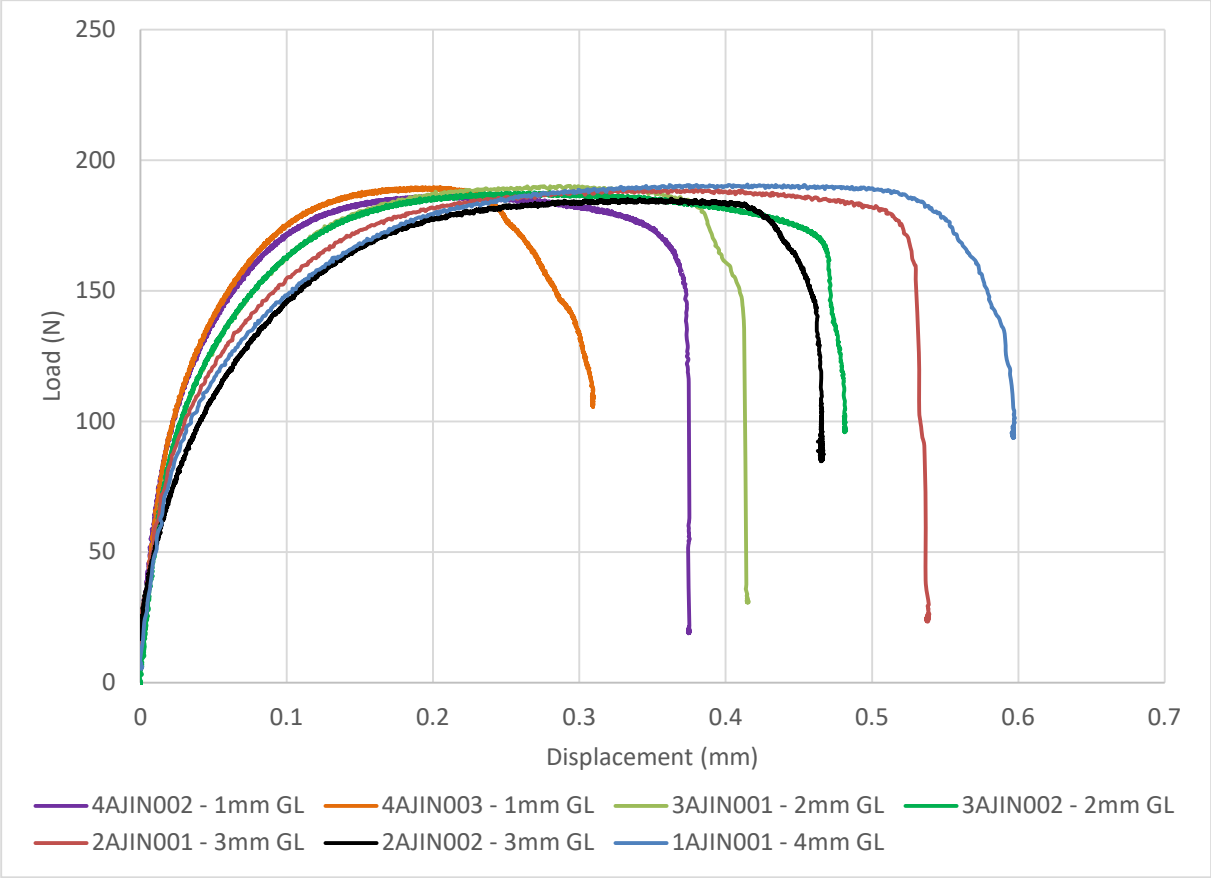

Figure 22 Load vs displacement results for all the tested 1 mm diameter single ligament samples

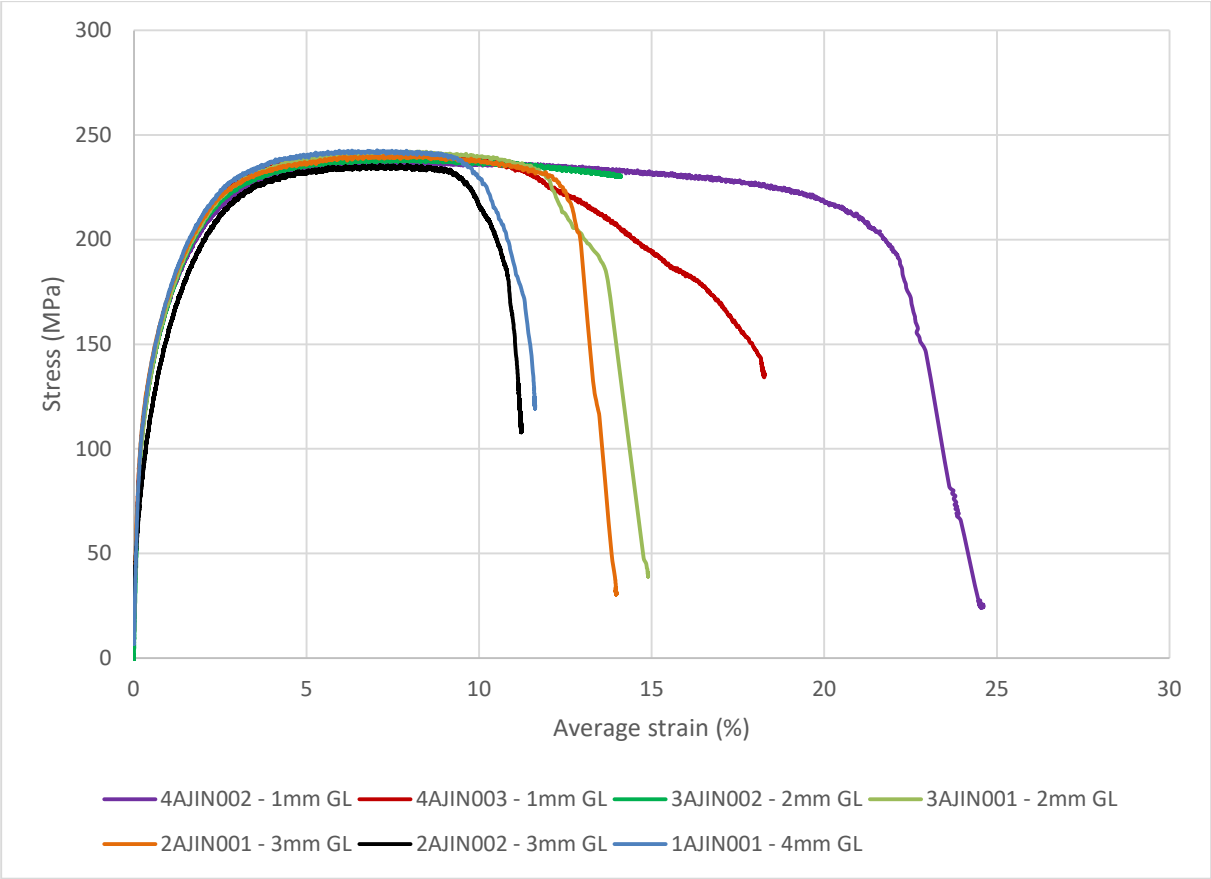

Figure 23 Stress vs average strain results for all the tested 1 mm diameter single ligament samples

Using the two sets of strain data for each test, it is possible to determine the degree of bending strain as a function of applied stress (or load) during the test. The difference in the measured strain between the front and back face of the test piece is shown in Figure 24. This shows good agreement between the two faces up to a stress of approximately 60 MPa. This is the point where the material starts to plastically deform after yielding as shown in Figure 23 and in Figure 25. The actual amount of bending strain introduced into the test piece has been calculated from this data and is shown in Figure 26. This shows that the degree of (relative) bending strain is high at very low loads and reaches a level of around 10% on average between the data sets becoming greater as the material yields and plastically deforms. Bending strain generally is more problematic on dynamic fatigue testing and will influence the fatigue life of materials [16,17,18] but is less of a problem in monotonic axial tensile testing. However, this degree of bending strain during the main elastic loading of the lattice single ligament test pieces is relatively low and within expected limits.

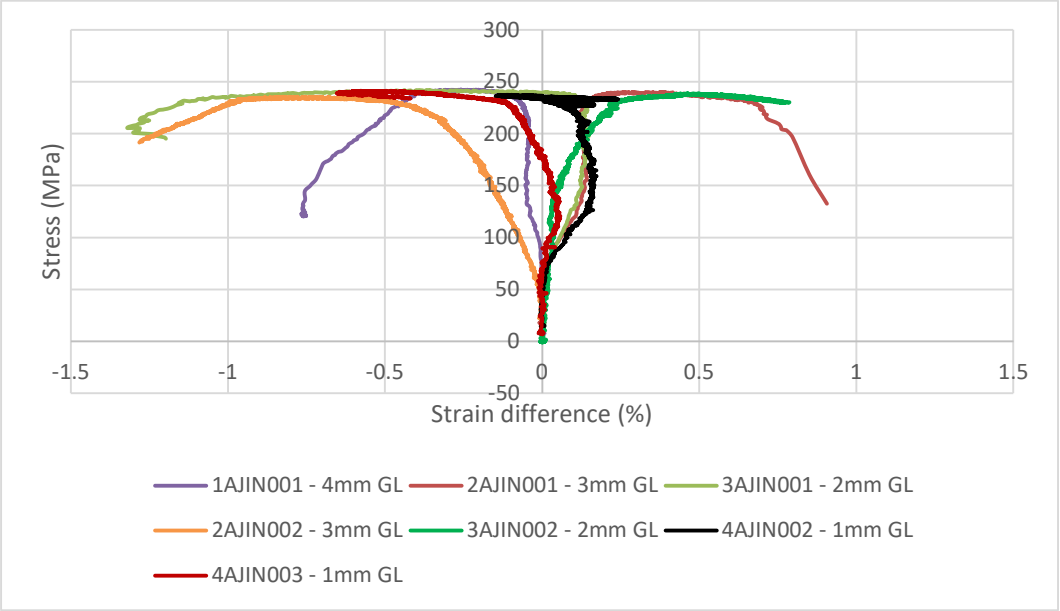

Figure 24 Difference in the measured strain on the front and back face of the test piece

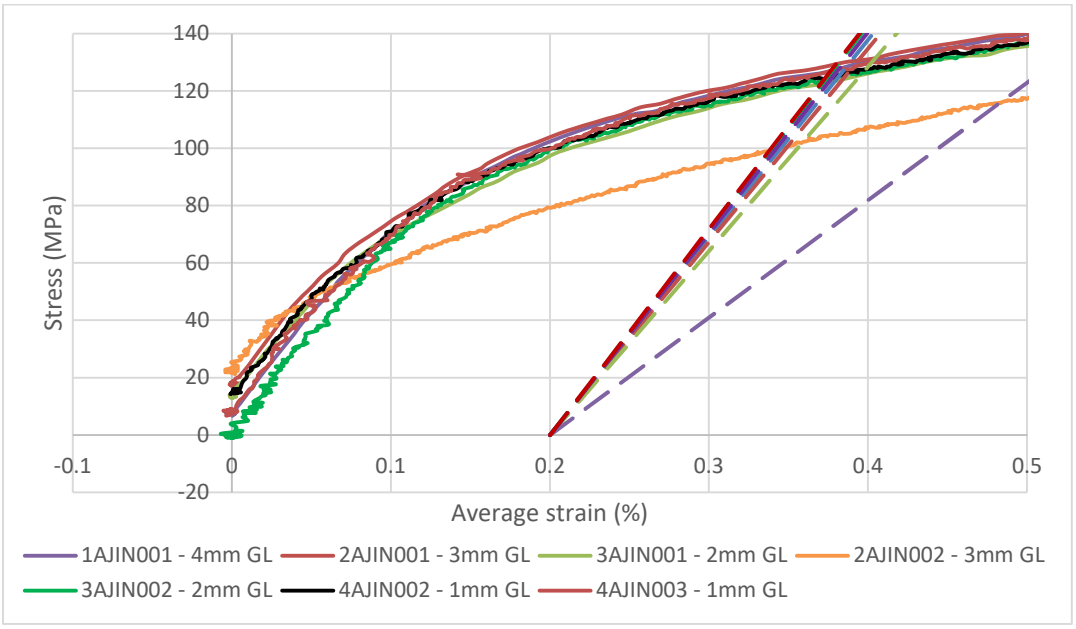

Figure 25 Expanded view of the stress vs strain elastic region data from Figure 23 with 0.2% yield stress construction lines

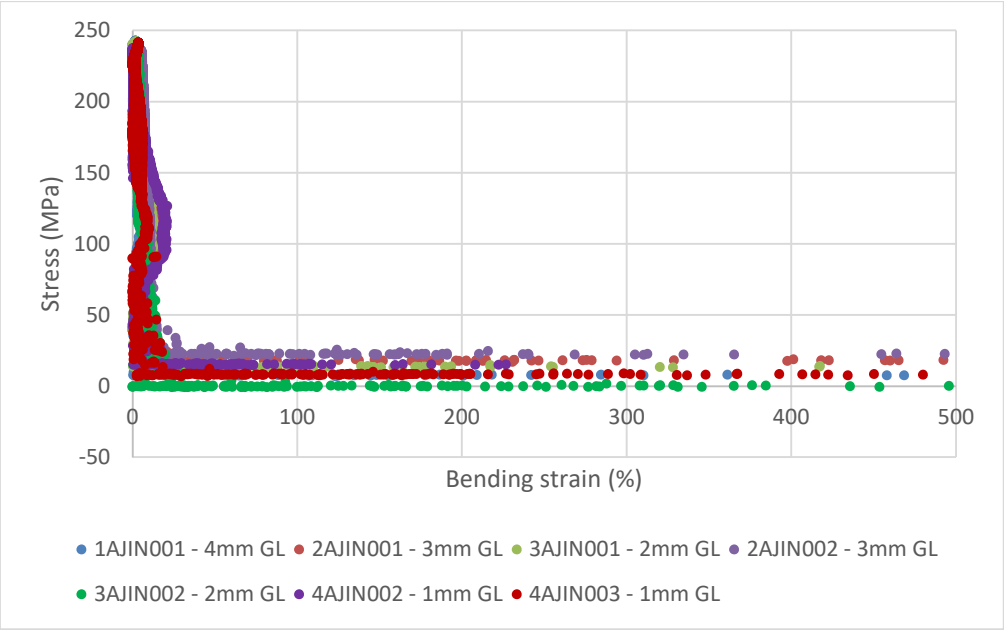

Figure 26 Relative bending strain as a function of applied stress

The results of the analysis of the stress-strain data are presented in Table 1, which shows the elastic modulus, yield stress and ultimate tensile stress values.

Table 1 Summary results for the single ligament tensile tests

Sample ID	Elastic Modulus*, GPa	Yield Stress, MPa	Ultimate Tensile Stress, MPa	Sample Gauge Length, mm
1AJIN001	69.0	128.5	242.8	4
2AJIN001	67.4	130.7	240.4	3
3AJIN001	64.3	125.5	242.5	2
2AJIN002**	40.9	116.1	235.9	3
3AJIN002	71.5	124.7	239.1	2
4AJIN002	70.3	124.8	237.8	1
4AJIN003	72.0	126.8	241.5	1
Average	69.08	125.3	240	
Standard Deviation	2.88	4.60	2.54	
Coefficient of Variation	0.04	0.04	0.01	

* calculated over a strain range of 0.01 to 0.05% for a nominal 1 mm ligament diameter
** outlier and excluded from modulus calculations

3.1.3 In-situ Micro Test System

In conjunction with the single ligament tensile tests conducted in the universal test system, a small number of tests were conducted using an in-situ micro test system. These measurements were performed using a Deben Microtest 5000 system with 5 kN load cell (Figure 27) inside a Tescan MIRA SEM (Figure 28). A close-up view of the single ligament test piece mounted in the Deben test system is shown in Figure 29.

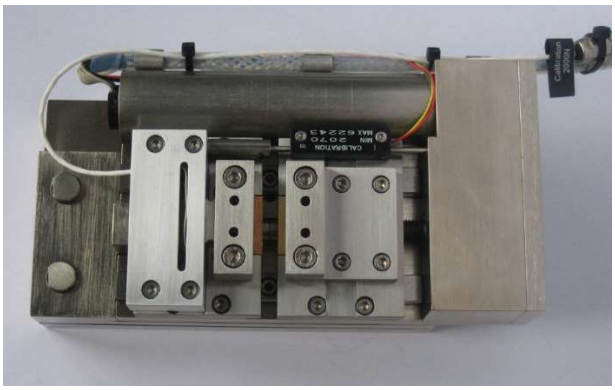

Figure 27 Deben Microtest 5000 system

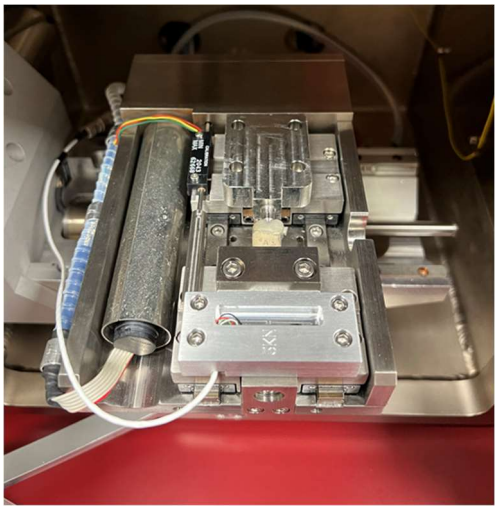

Figure 28 Micro test stage inside the Tescan MIRA SEM

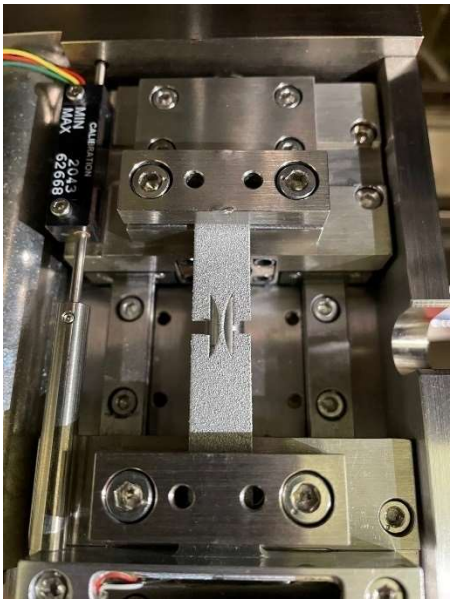

Figure 29 Close up view of test piece mounted in the Deben test system prior to testing

3.1.4 In-situ Micro Test System Results

The Deben test rig used displacement control during the test and applied the displacement at a rate of 0.1 mm/min. Four tests were conducted using single ligament test pieces with a nominal diameter of 1 mm and gauge lengths of 1, 2, 3 and 4 mm (AJIN005, 3AJIN005, 2AJIN005 and 1AJIN005 respectively). The results of these tests are compared to the tests conducted on the universal test system, details in section 3.1.1 and 3.1.2, and shown in Figure 30. Examination of the Deben data shows what appears to be two distinct slopes in the initial elastic portion of the curve. It is possible to offset the data such that the second slope can be overlaid onto the universal test system data, shown in Figure 31. If we assume the cross-sectional area based on 1 mm nominal diameter, then the stress vs strain in the ligament can be plotted based on displacement values for the applied strain in the micro test results, Figure 32.

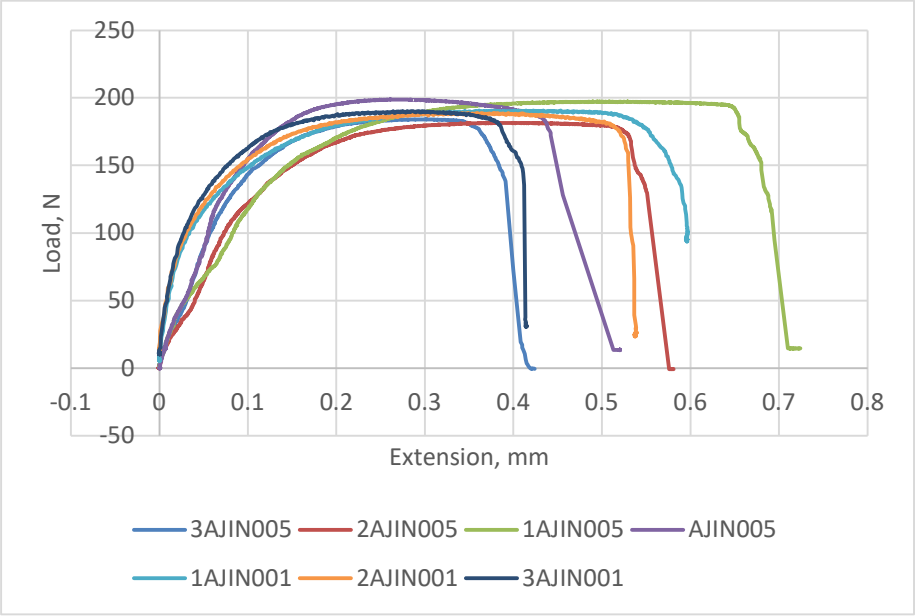

Figure 30 Comparison of load vs displacement data for the single ligament tests conducted in the universal test system and the Deben micro test system

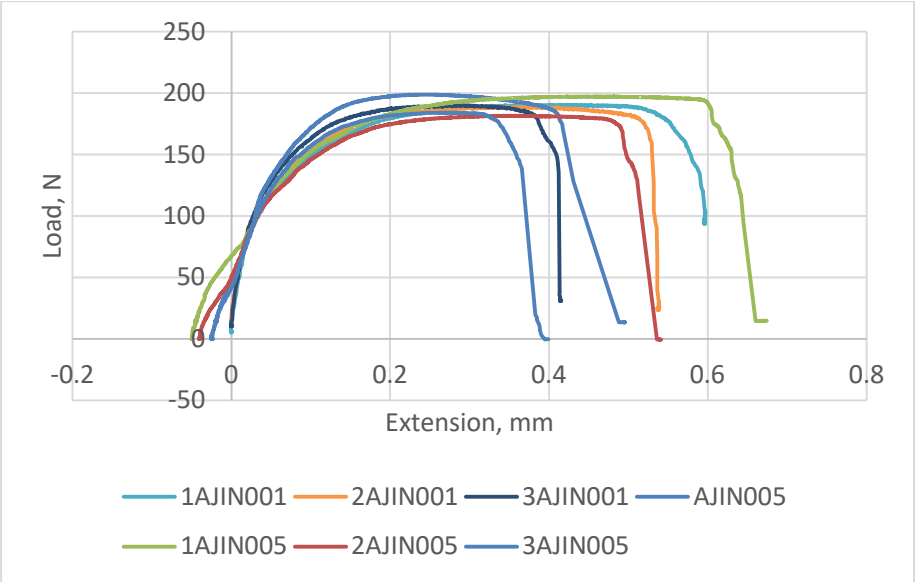

Figure 31 Comparison of load vs displacement data for the single ligament tests conducted in the universal test system and the Deben micro test system, Deben data offset to align with universal test system data

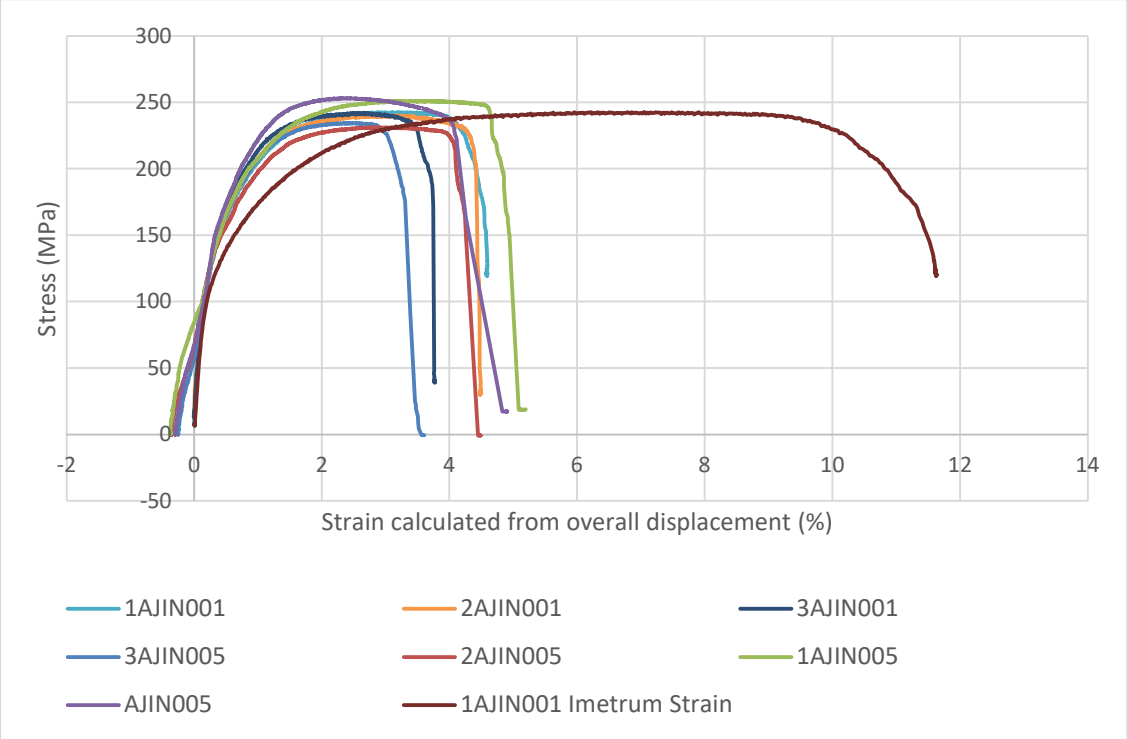

Figure 32 Comparison of stress vs strain for the single ligament tests conducted in the universal test system and the Deben micro test system, Deben data offset to align with universal test system data

The strain data in Figure 32 has been compared with the non-contact strain data measured on the Imetrum to provide an indication of the differences between strain based on overall displacement and strain from measurements from the gauge length. The strain data from the universal test system has also been calculated based on crosshead displacement for the purposes of comparison in Figure 32 and Figure 33, which is an enlarged view of the elastic region of Figure 31. This suggests that there is a systematic offset in the displacement, further

reinforced by Figure 34, which shows the offset in displacement as a function of the single ligament gauge length. This is discussed further in section **Error! Reference source not found.**.

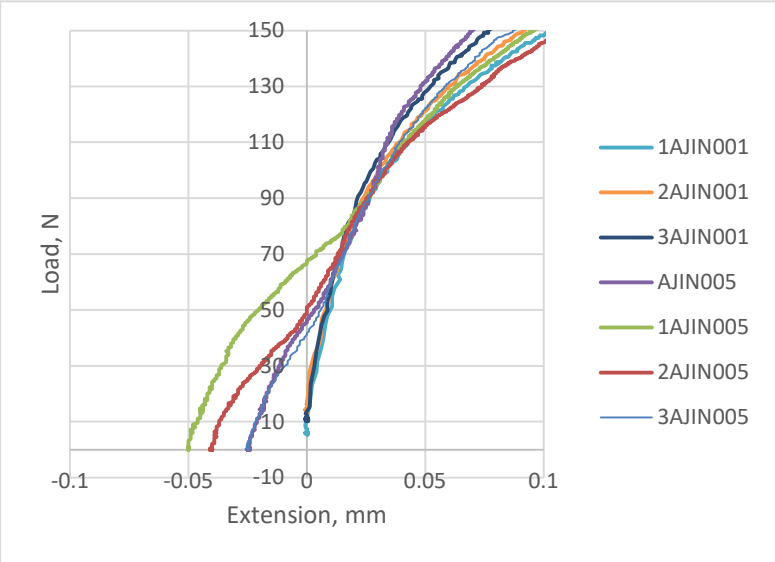

Figure 33 Enlarged view of the elastic region of the load vs displacement plot shown in Figure 31

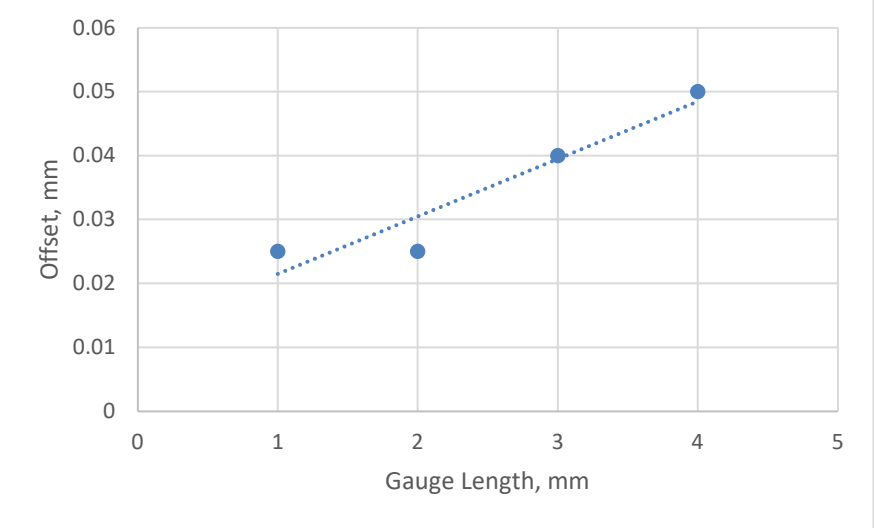

Figure 34 Offset in the displacement as a function of sample gauge length

One of the single ligament test pieces was selected for scanning electron microscopy (SEM) imagining. Both the top and bottom halves of the fracture surface were examined in the SEM and are shown in Figure 35 and Figure 36 respectively. The failure surfaces show that the fracture occurred through ductile failure. These images also show spheres of powder material adhered to the outer wall of the ligament (Figure 35(a) and below Figure 36(a)). Pore holes can be observed in the fracture surface indicated by arrows in Figure 35(b) and visible in Figure 35(c) and Figure 36(b) and (c).

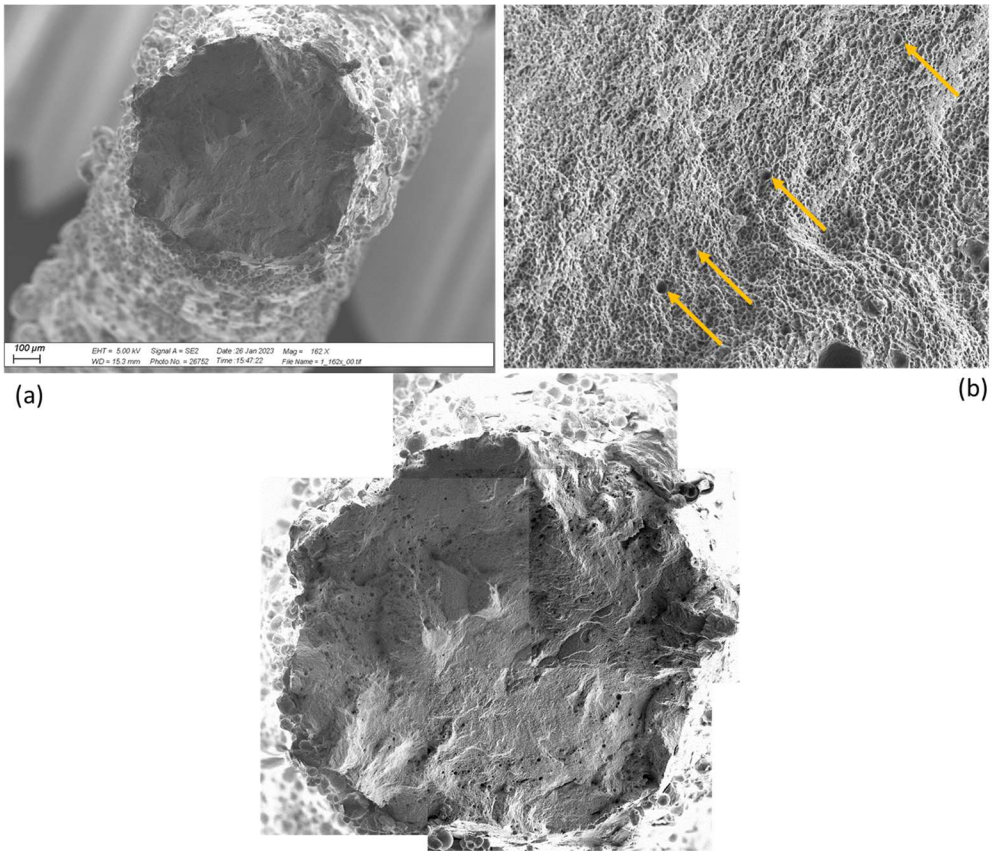

Figure 35 SEM images of the fracture surface for a single ligament test piece (top half)

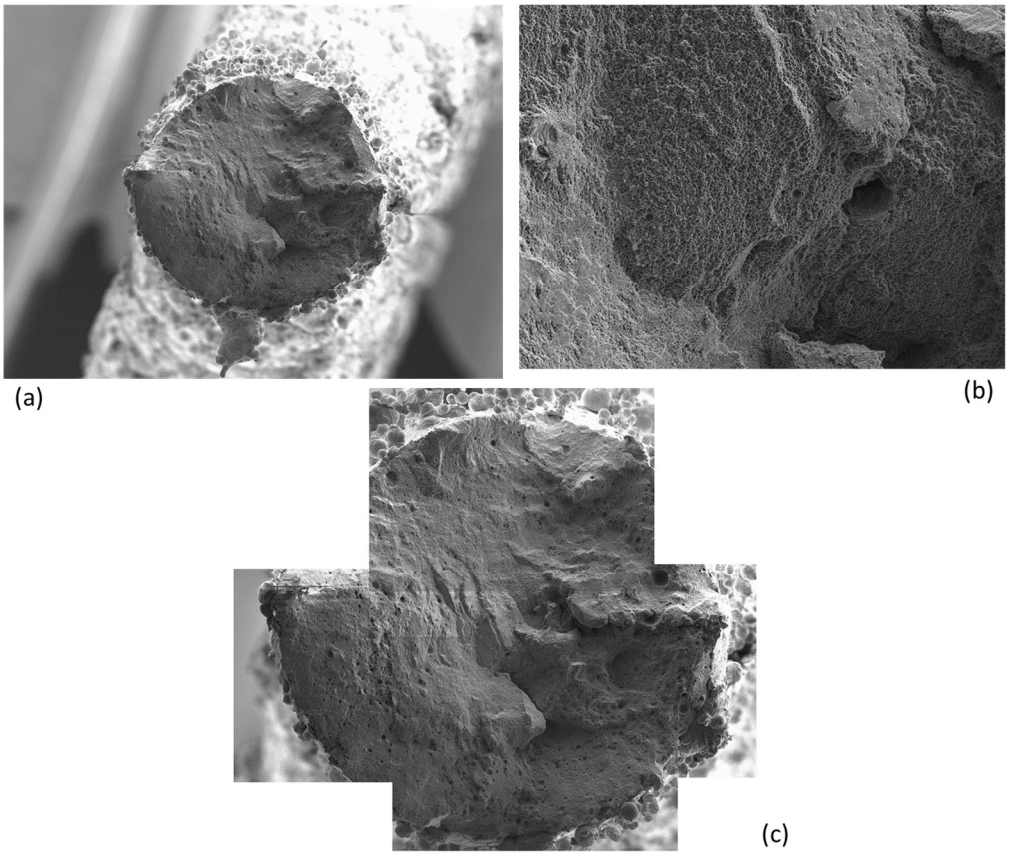

Figure 36 SEM images of the fracture surface for a single ligament test piece (bottom half)

3.2 LATTICE UNIT CELL

The same test piece design was adopted for the lattice unit cell samples. The aim was to measure the strength and mechanical properties of a single lattice cell, and to facilitate this the test pieces were manufactured in a chain of nine cells. Two different strut diameters were used 0.30 mm and 0.25 mm as shown in Figure 37, using a relatively simple BCC unit cell geometry. The 0.25 mm lattices were formed from a chain of 3 cells of 0.3 mm diameter at each grip end for strength with the central 3 unit cells reduced to 0.25 mm diameter. Testing was conducted in the universal test system using a displacement rate of 0.1 mm/min using a 1 kN load cell. As with the single ligament test piece, the sample was very carefully mounted and gripped into the test machine (this was done without specimen protect engaged as this feature was causing jitter as the system struggled to control at low load levels) before the side supports were cut through. Repeat tests were conducted on the two lattice designs (0.3 mm and 0.25 mm diameter) and an example of the results, showing applied load and displacement, are provided in Figure 38. This shows that as expected the larger lattice struts were able to carry higher loads reaching ~32 N, whilst the thinner struts were only able to carry ~8.5 N. An approximation has been made of the load bearing cross sectional area of the lattice, based on the nominal strut diameter, and the corresponding stress calculated for each test. The plot of nominal stress vs displacement is shown in Figure 39, with the 0.3 mm lattice struts plotted on the left-hand axis and 0.25 mm strut on the right-hand axis. This shows that yield for the two lattice structures occurred at a similar applied displacement and that the 0.3 mm lattice had an ultimate tensile strength (UTS) of 112 MPa and the 0.25mm lattice a UTS of 42.7 MPa. Non-contact strain measurement (Imetrum) was used during these tests setting the gauge length markers over three distinct regions. The first was to consider the ‘global’ strain on the test piece by considering the gauge length to be the point between the lattice and the end tab section, shown in Figure 37 as the yellow lines. The second gauge length considered a reduced range closer to the expected failure, either the central 5 unit cells for the 0.3 mm struts or the central 3 unit cells for the 0.25 mm struts, shown in Figure 37 as the red line. Finally, the third region considered the central 3 unit cells for the 0.3 mm diameter struts or the single central unit cell for the 0.25 mm diameter struts, shown in Figure 37 as the green line.

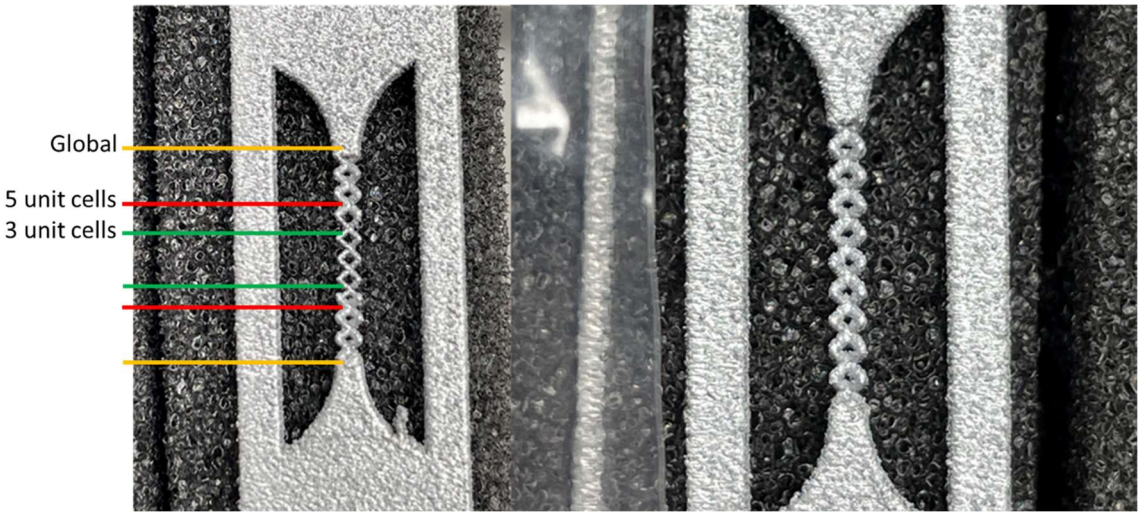

Figure 37 Lattice unit cell test pieces, 0.25 mm diameter on the left and 0.3 mm diameter on the right

All the result plots (Figure 38 to Figure 41) show a stepped failure of the lattice test piece. Observation of the lattice structure during the tests showed that failure was not apparent across the whole lattice structure with little obvious elongation or deformation on the adjacent unit

cells beyond the one that ultimately resulted in failure. This can be seen in Figure 42 and Figure 43, which show the failed specimens for the 0.3 mm and 0.25 mm lattices respectively.

Deformation and final failure are focussed on a single lattice unit cell, as one might expect for this particular layout and geometry, with failure occurring in one lattice strut after the other until the whole sample fails. The actual failure location with the lattice cell was seen to vary, with failure occurring in the centre section of a strut in some cases whilst others would fail closer to the node or apex.

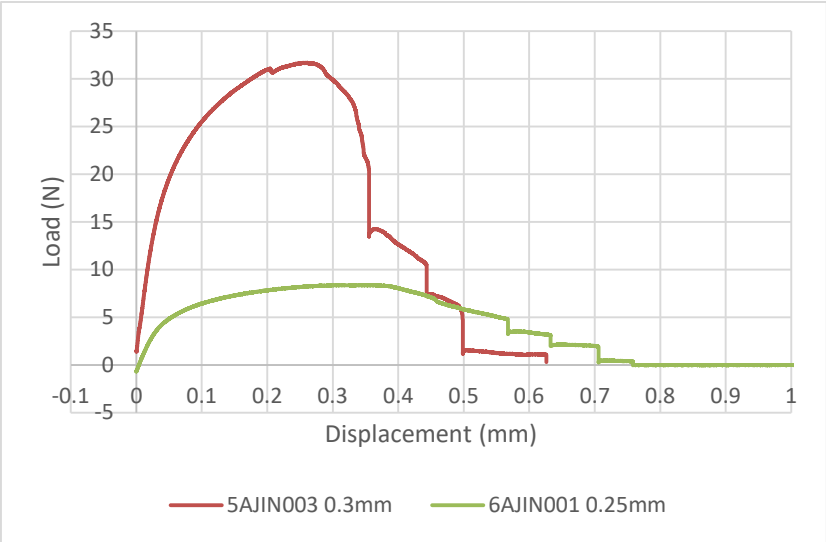

Figure 38 Load vs displacement for the 0.3 mm and 0.25 mm lattice test pieces

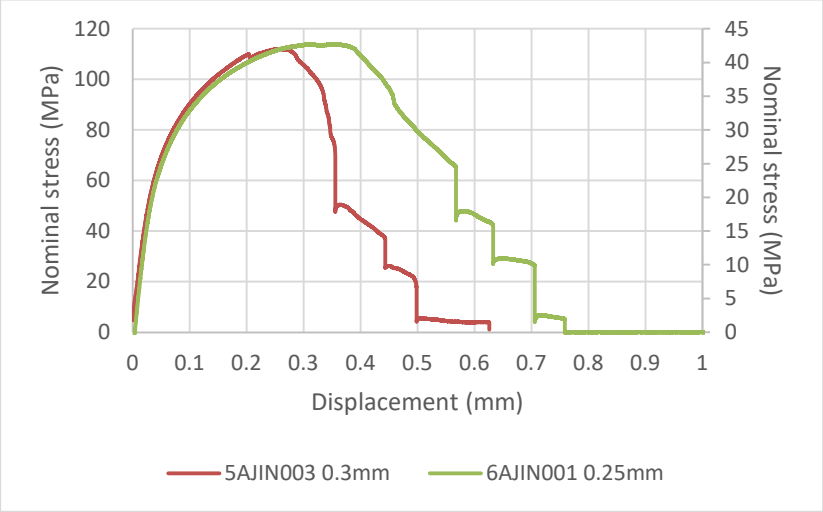

Figure 39 Nominal stress vs displacement for the 0.3 mm and 0.25 mm lattice test pieces

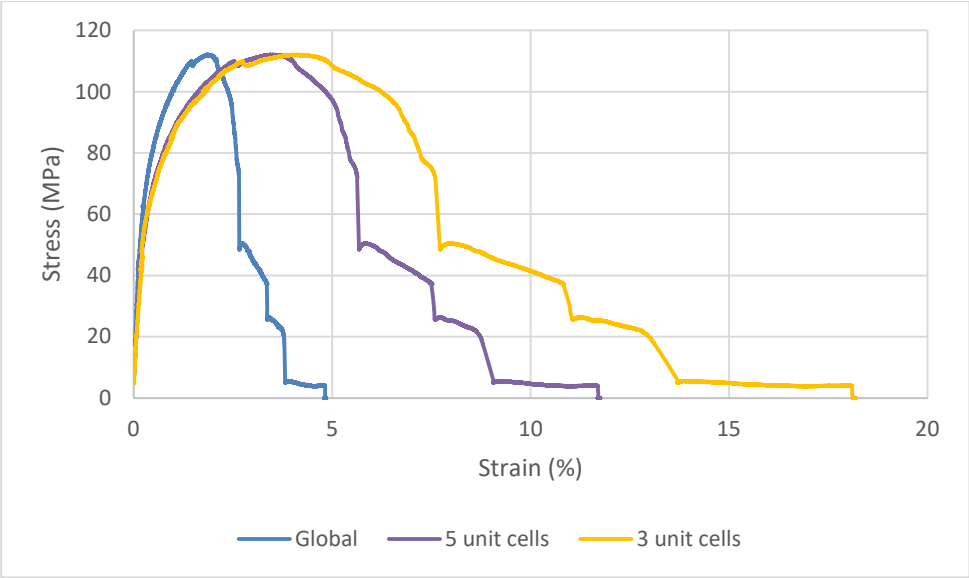

Figure 40 Nominal stress vs strain plots for the 0.3 mm diameter lattice test piece with the strain measured by the Imetrum over different gauge length ranges

Figure 40 shows the stress vs strain response for the 0.3 mm lattice. In this case the failed lattice cell was within the smallest analysis field of view of the Imetrum, and so in each of the traces we observe the sequential failure of the lattice struts. This is not the case with the 0.25 mm diameter lattice test piece shown in Figure 41. In this case the global and 3 unit cell analysis windows capture the failure instances, but the central unit cell was not the failure cell and only shows the elastic/plastic response of a lattice cell without the sudden strain increases seen in the other two traces. The failed lattice cell in each instance is shown in Figure 42 and Figure 43. It is particularly evident in Figure 43 that the failed lattice cell has undergone extensive elongation and 'straightening' of the cell compared to the cells in the chain above and below it.

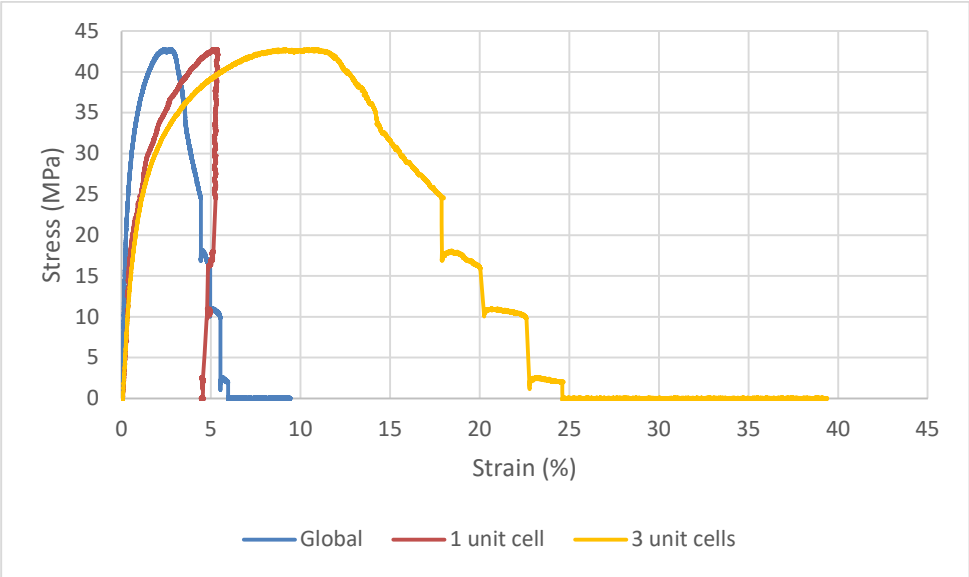

Figure 41 Stress vs strain plots for the 0.25 mm diameter lattice test piece with the strain measured by the Imetrum over different gauge length ranges

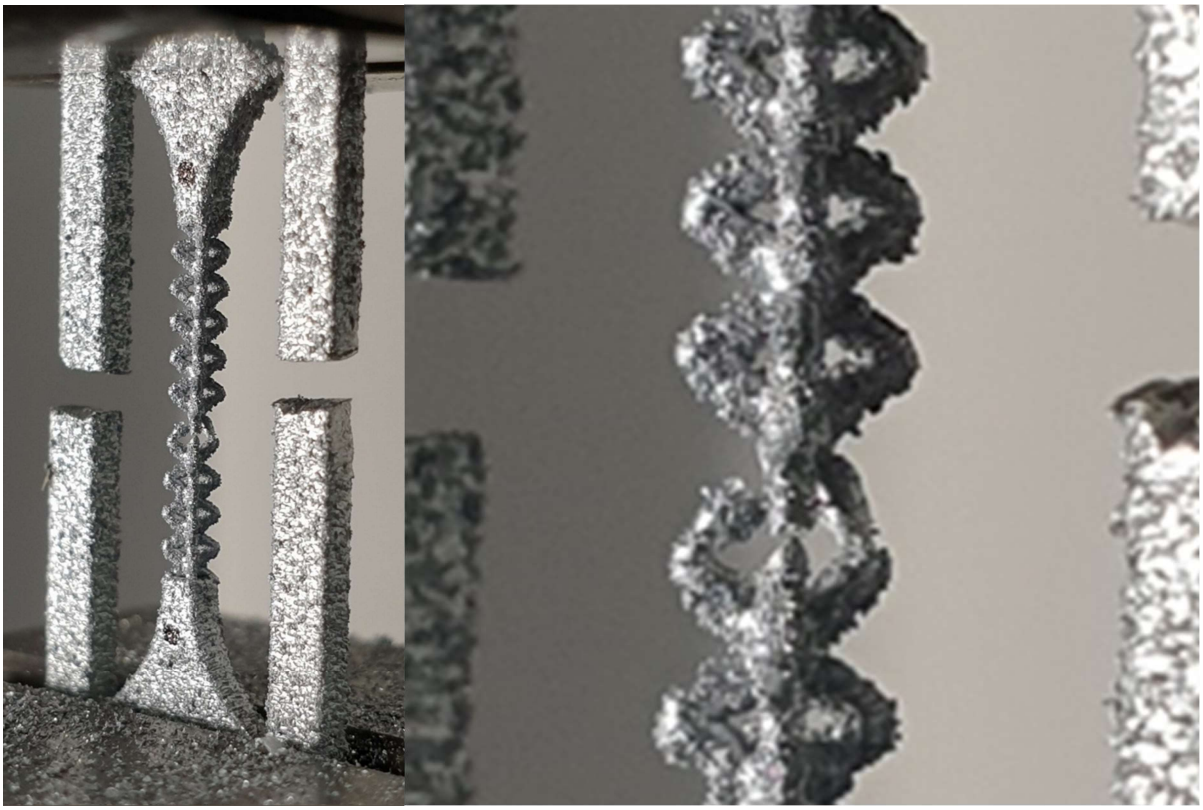

Figure 42 0.3 mm lattice test piece after testing

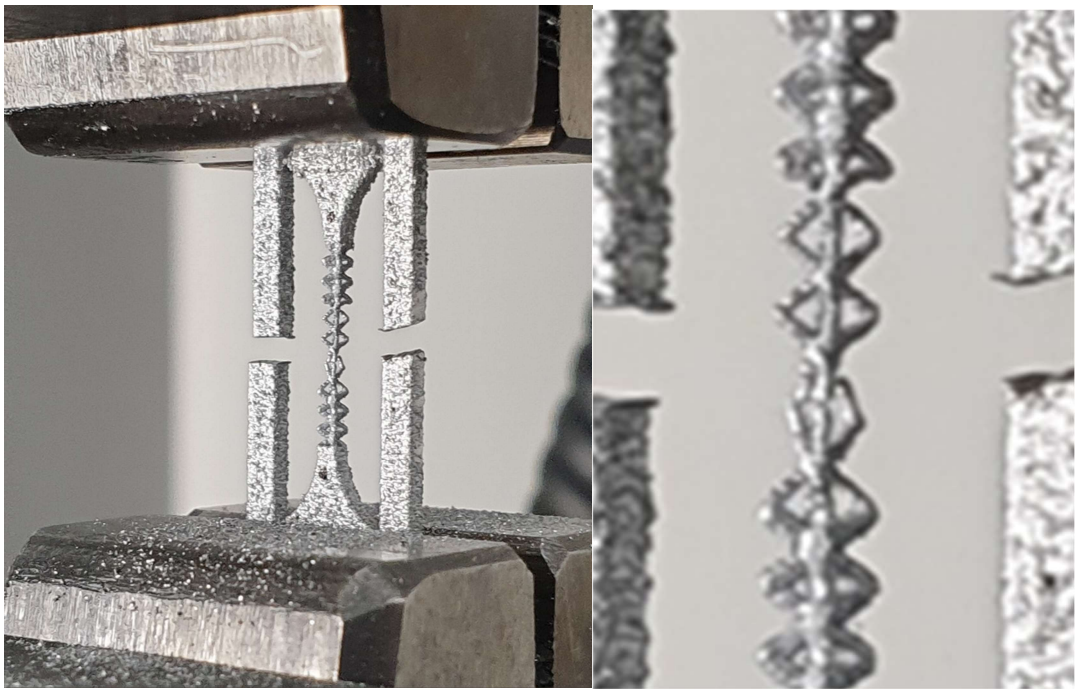

Figure 43 0.25 mm lattice test piece after testing

4 FINITE ELEMENT MODELLING

4.1 SINGLE LIGAMENT MODEL

Finite element analysis (FEA) software package Abaqus was used to model the behaviour of a ligament sample. The surface tessellation model (STL) file created for printing the parts, was used to assist in generation of the FE geometry. When STL files are imported into Abaqus CAE, the Abaqus pre and post processor, they are created as orphan meshes which aren't always easy to manipulate and mesh. There are various tools available to allow the geometry to be improved, but as the geometry was fairly simple, the imported orphan mesh was used as a template to generate a 2D geometry in Abaqus CAE. The central region of the ligament sample has a circular cross-section, so a 3D swept geometry was created from the 2D geometry. This was then cut down to create the final sample geometry, see Figure 44.

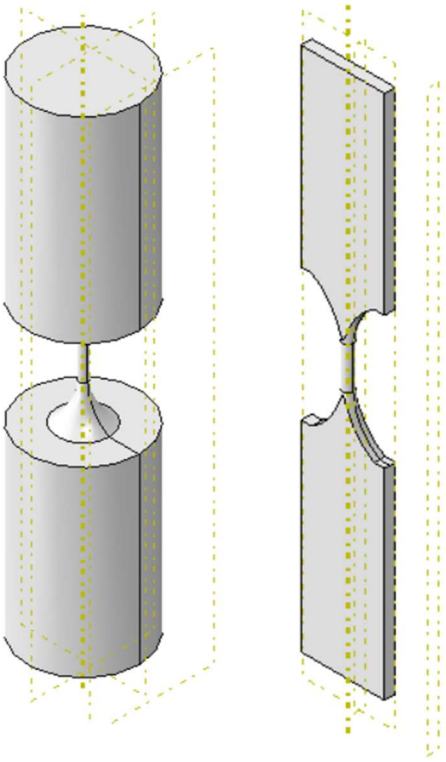

Figure 44 Development of the ligament geometry in Abaqus CAE

This process has been repeated for three different diameter specimens (d = 0.5, 0.75 and 1 mm) with the gauge length region being 4 x d in each case, see Figure 45.

Grip regions were created, and the lower grip region was fully constrained. The top grip region was constrained in the x- and z-directions. All nodes in the top grip region were tied to a single node in the y-direction by an equation. This meant that the overall displacement could be applied to this single node, and this node could be used to output the total reaction force. These boundary conditions are shown in Figure 46(a). A displacement of 0.225 mm was applied to the 0.5 mm diameter geometry and 0.3 mm displacements were applied to the 0.7 mm and 1 mm diameter ligaments.

A fine mesh was created on the main section of the sample with a coarser mesh in the grip regions, see Figure 46(b), using quadratic tetrahedron, type C3D10 elements. A node set

containing gauge nodes was also created, Figure 46(c), to enable strain calculation from the parallel sided region.

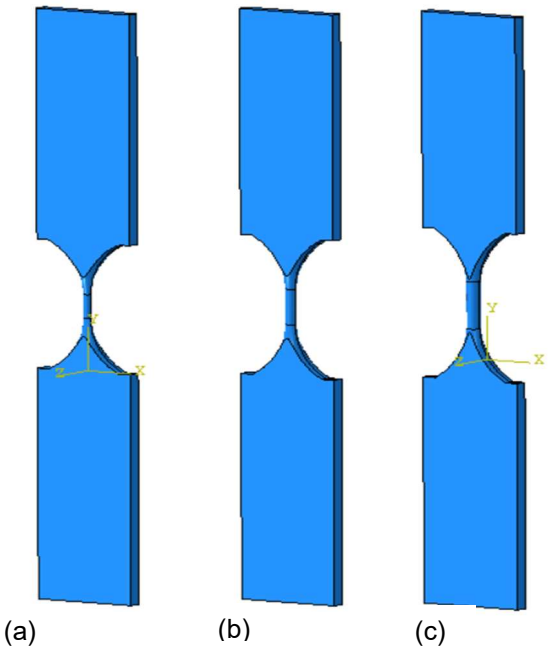

Figure 45 Final geometries for ligaments with diameters of (a) 0.5 mm, (b) 0.75 mm and (c) 1 mm

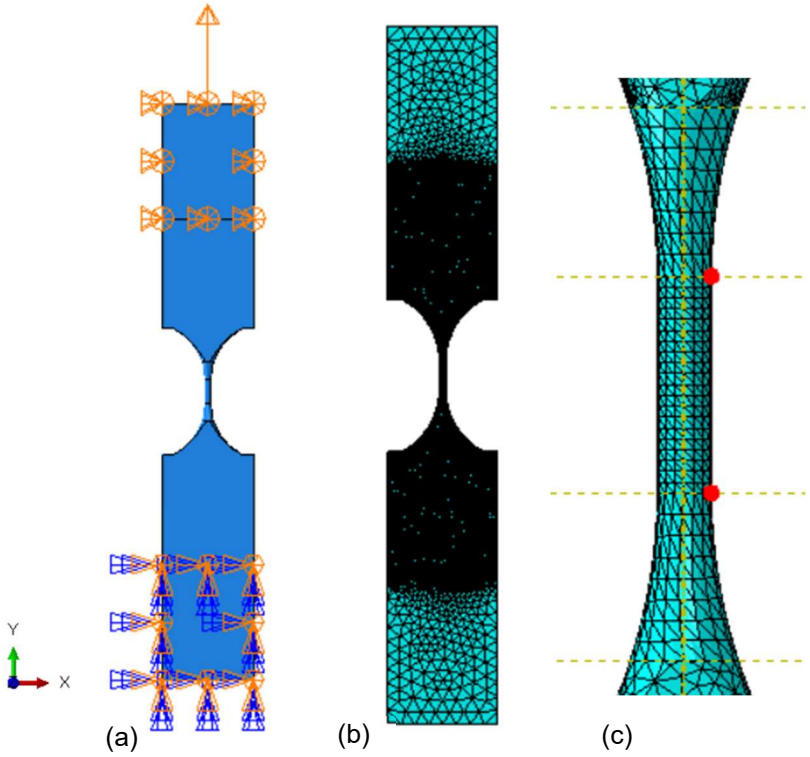

Figure 46 Ligament geometry showing(a) boundary constraints, (b) mesh and (c) location of gauge nodes

The material properties were obtained from the single ligament tests, see Figure 21, using data from the 1 mm diameter, 3 mm gauge length specimen. An elastic-plastic material model was used to represent the AlSi10Mg alloy, with a Young's Modulus of 67446 MPa and a Poisson's ratio of 0.33. Elastic-plastic models require a hardening curve of stress vs plastic strain to define the plastic behaviour of the material. The hardening curve obtained from the stress-strain data is shown in Figure 47.

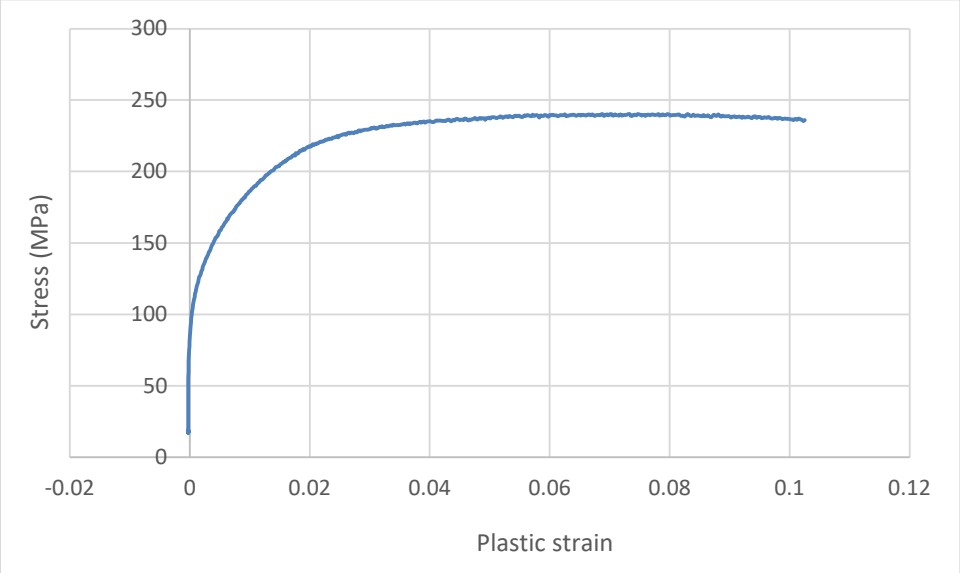

Figure 47 Hardening curve defining plastic behaviour of the AlSi10Mg alloy

The predicted force-displacement curves for the three geometries are shown in Figure 48 and the corresponding stress-strain plots are given in Figure 49. As expected, there are clear differences between the force-displacement plots with the larger diameter ligament sustaining the largest force. The stress-strain plots are consistent with each other and represent the material response described within the FE models material definition.

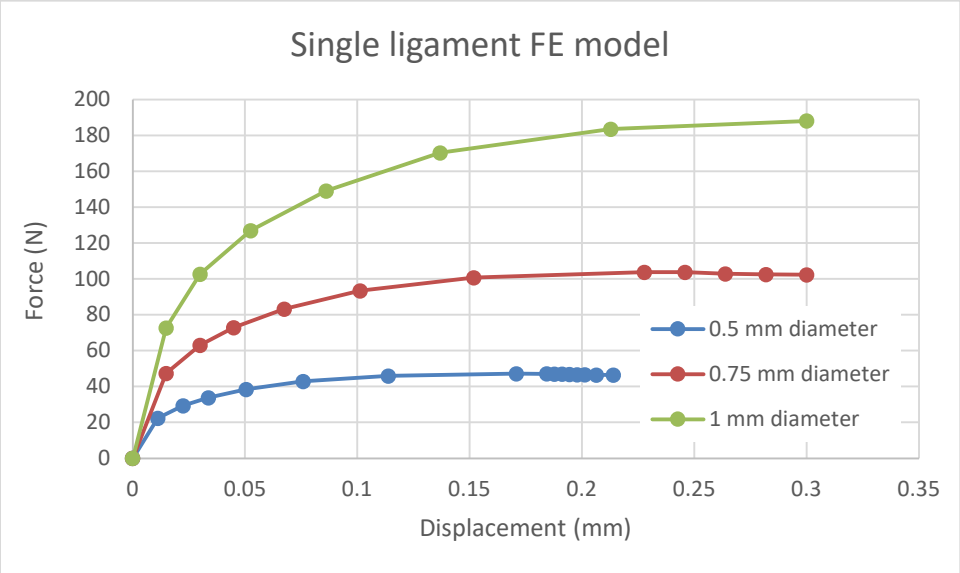

Figure 48 Predicted force-displacement plots for the three different diameter ligament models

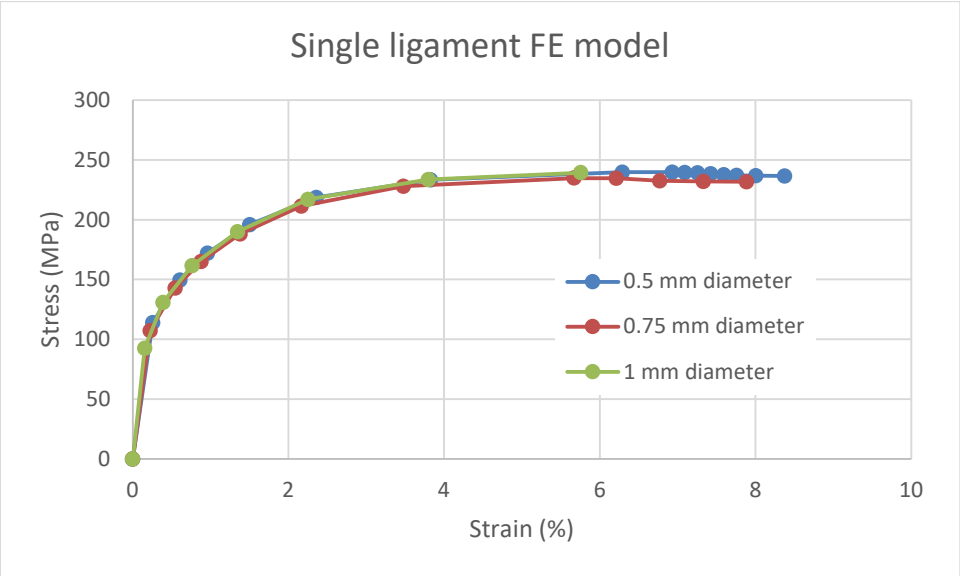

Figure 49 Predicted stress-strain plots for the three different diameter ligament models

The predicted load-displacement response of the 1 mm diameter geometry has been compared to experimental data from 1 mm diameter specimens. The FE prediction correlates well with the measured behaviour, Figure 50.

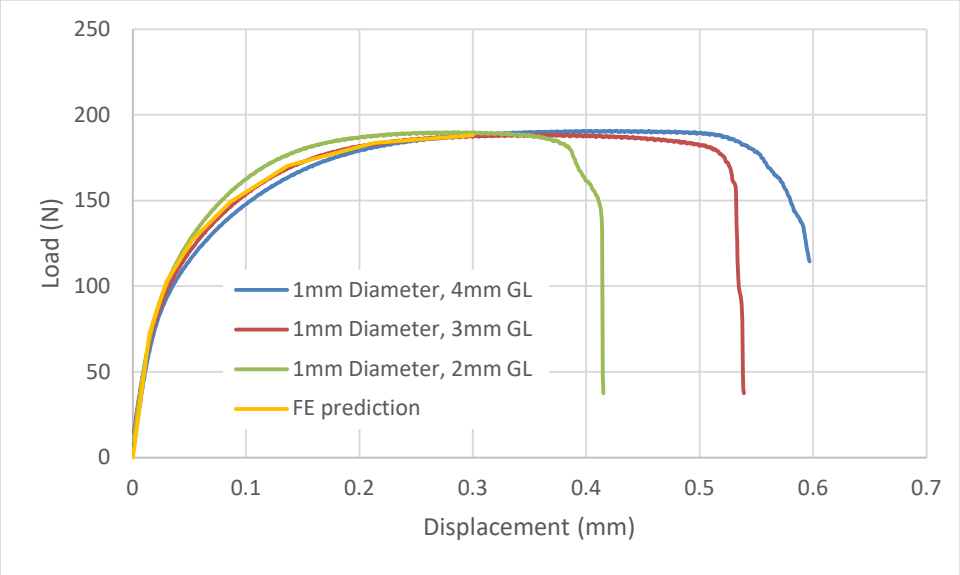

Figure 50 Comparison of FE predicted load-displacement and experimental data for a 1 mm diameter ligament specimen

4.2 LATTICE MODEL

Initially a single unit cell of the lattice structure was modelled before this was expanded into the full lattice structure. A surface tessellation model (STL) file created for printing the parts, was provided to aid the development of the FE model. Due to the issues with importing the STL file into Abaqus mentioned previously, this was used as a template to create a single unit cell. The dimensions of the ligaments were obtained from the STL imported orphan geometry and recreated using Abaqus CAE ensuring each strut was positioned exactly so they sat in the correct places to define the geometry. The ligament diameter was 0.3 mm, and the width of the unit cell was 1 mm, see Figure 51(a). The geometry was meshed with quadratic

tetrahedron, type C3D10, see Figure 51(b). The material data used for the previous ligament modelling was also used for the lattice modelling. Due to the smaller diameter of each of the struts in the single unit cell, an additional ligament model was created with a diameter of 0.3 mm to aid comparisons.

For the single unit cell model, boundary conditions were applied to the model to simulate tensile loading. The nodes on the flat faces of the left-hand side of the geometry were fully constrained. The x-direction movement of the nodes on the flat faces were tied to the displacement of a single node using an equation to allow output of the total force from this single node. The displacement of all nodes on these flat faces were constrained in the y- and z-directions, see Figure 52.

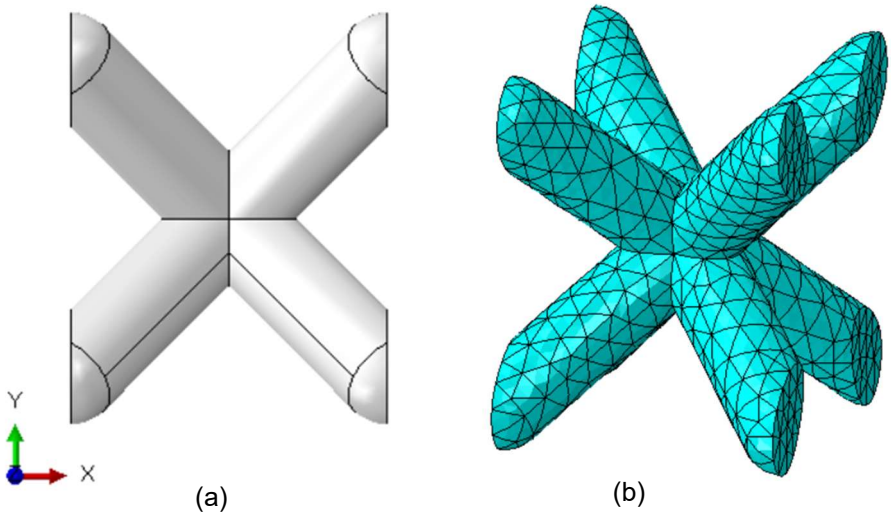

Figure 51 Single unit cell geometry (a) and meshed part (b)

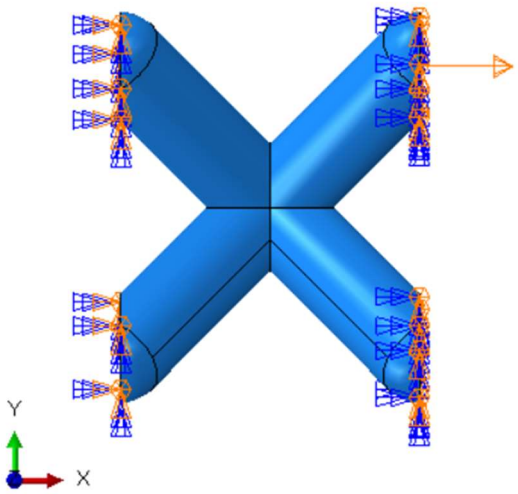

Figure 52 Boundary conditions applied to the single unit cell geometry

This single unit cell model was used as the basis of a multi-unit cell model that would correlate with the additively manufactured lattice sample. The mirror image tool was used to create a

line of 10 unit cells, see Figure 53(a). Boundary conditions were applied in the same manner as for the single unit cell geometry, see Figure 53(b).

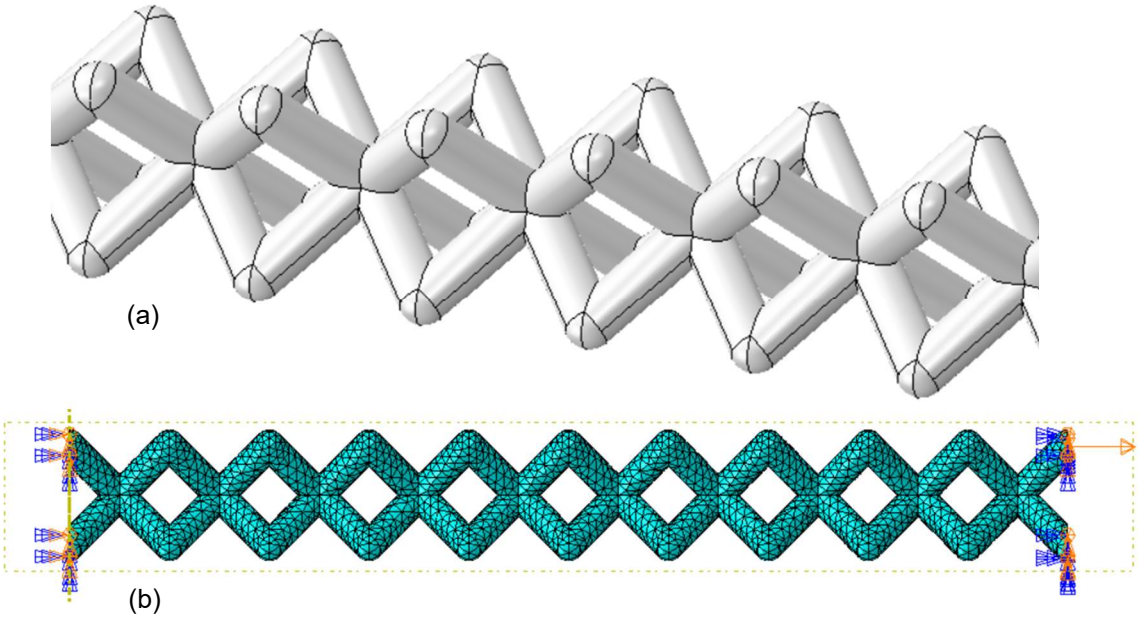

Figure 53 Lattice geometry (a) and meshed geometry showing boundary conditions (b)

This geometry was then used to create wider lattice structure models. This time a single width lattice 19 units long was used, with either 2 (Figure 54), 3 (Figure 55) or 4 (Figure 56) repeats of this lattice geometry. The models were set-up in the same manner as previously.

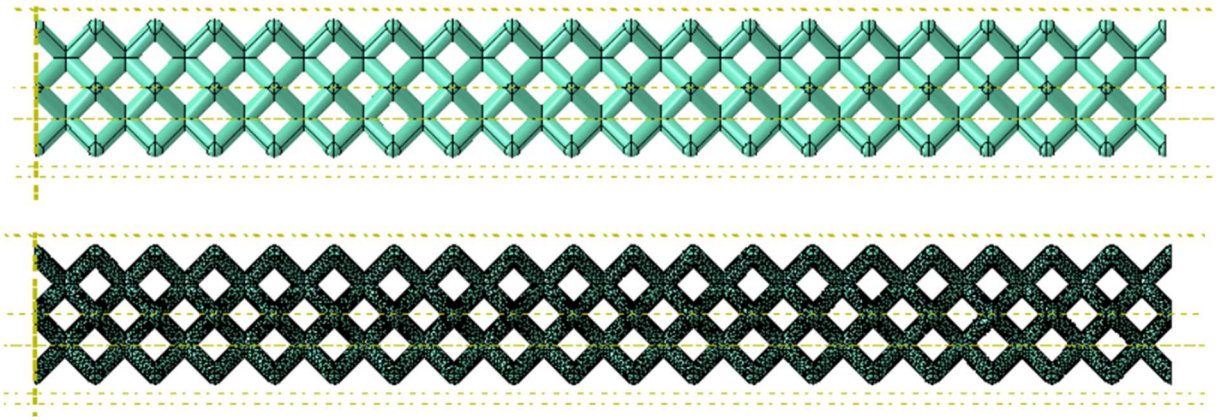

Figure 54 Geometry and mesh of 2-cell wide geometry

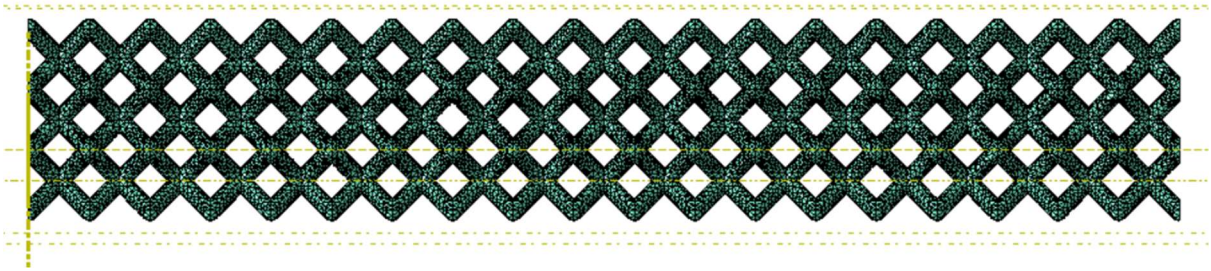

Figure 55 Mesh of 3-cell wide geometry

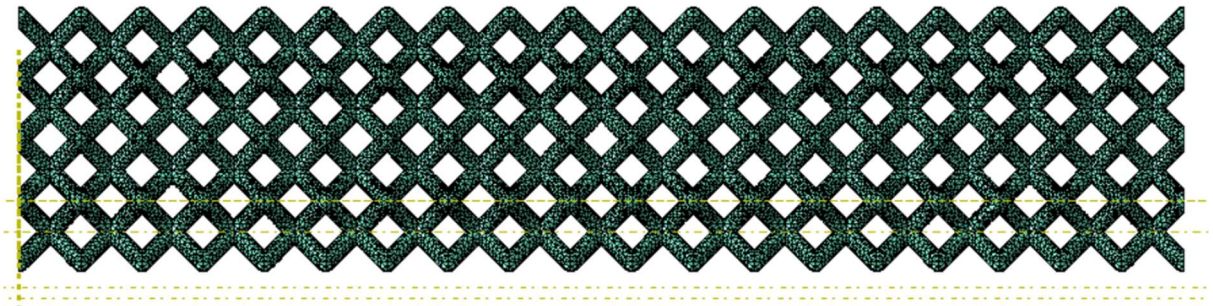

Figure 56 Mesh of 4-cell wide geometry

Figure 57 shows the force-displacement plots obtained from the analyses of the single unit cell and the single width lattice structure. The struts within these geometries are 0.3 mm wide so, for comparison, these results have also been plotted alongside the force-displacement plot obtained for the 0.3 mm ligament model. The single unit cell is stiffer and sustains a higher load than that of the single ligament model. In the full lattice structure, the predicted load is much lower, and the displacements are larger than the single unit cell model. The maximum loads for the full lattice structure are higher than those predicted for the single ligament model.

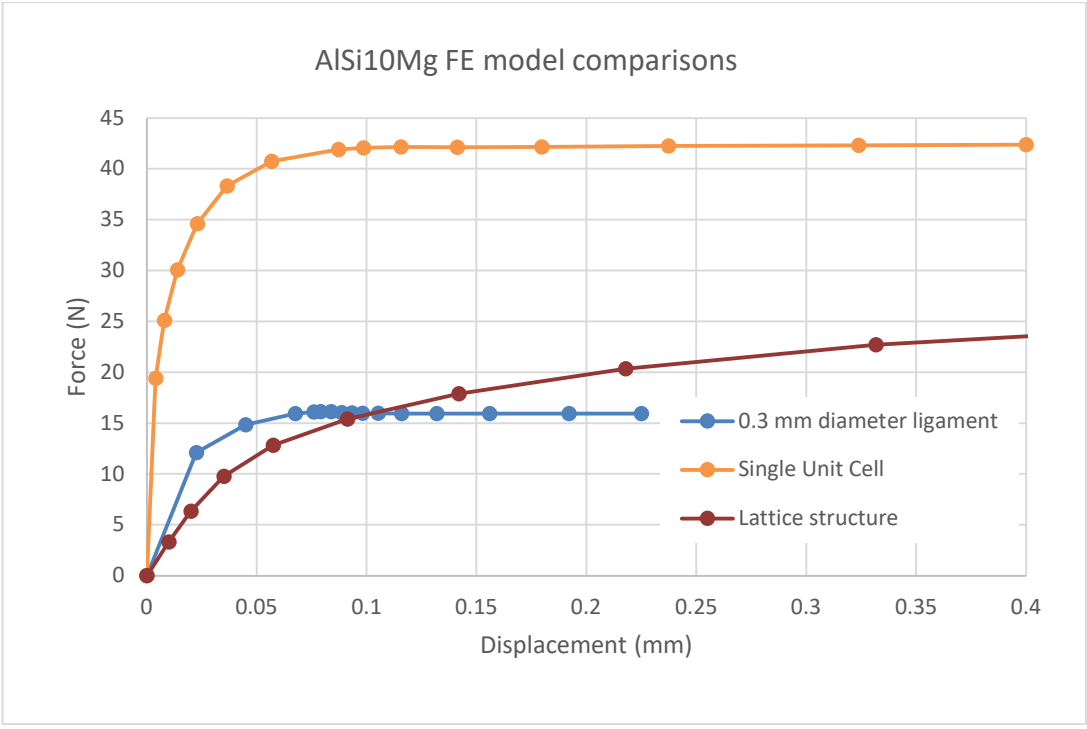

Figure 57 Comparison of the force-displacement plots obtained from the single unit cell, single width lattice structure and the 0.3 mm diameter single ligament model

In both the single unit cell and the lattice structure, there is a substantial shape change with the struts deforming in a scissor-type action, see Figure 58. In the case of the single unit cell, the structural response is stiffer than that for both the ligament and lattice models. But once this cell geometry is repeated multiple times to create the lattice structure, this scissoring/strut alignment has a more substantial effect on the load response of the sample.

The elongation of the unit cells making up the lattice geometry can be seen clearly by comparing the deformation of individual cells in the lattice structure. Figure 59 shows an elongation of the diamond-shape opening at the centre of the struts.

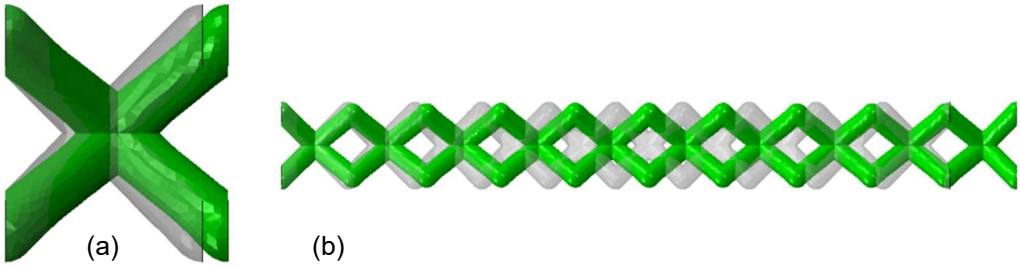

Figure 58 Deformed geometry (green) superimposed on the original geometry (grey) for (a) the single unit cell and (b) the lattice geometry

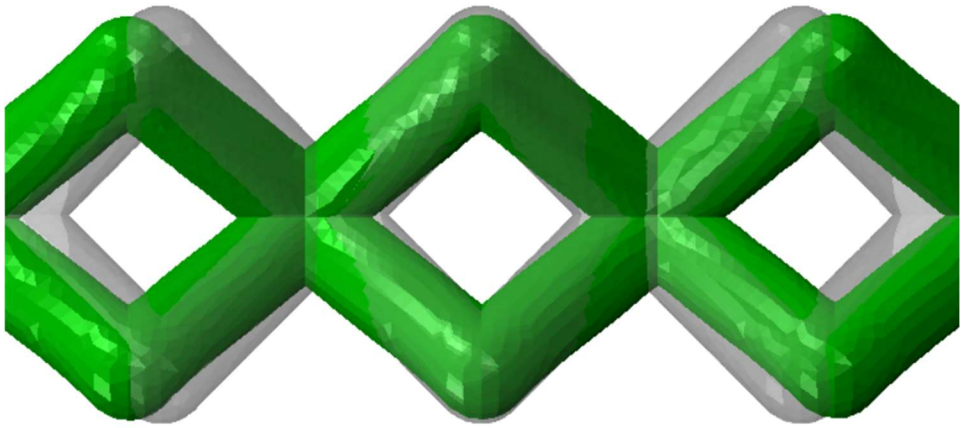

Figure 59 Close up showing the change in shape of the cell geometry, deformed geometry (green) superimposed on the original geometry (grey)

The force-displacement predictions for the lattice structures with different cell widths are shown in Figure 60. As expected, the response of the structure is width dependent, with the wider structures being able to sustain more load at an equivalent displacement. The longer number of cells within this model (19 compared to 10 unit cells for the standard lattice geometry) has reduced the stiffness of the geometry. This can be seen when comparing the force-displacement plot for the 10 unit cell lattice structure in Figure 57 with the 19 unit cell, 1 cell wide response in Figure 60.

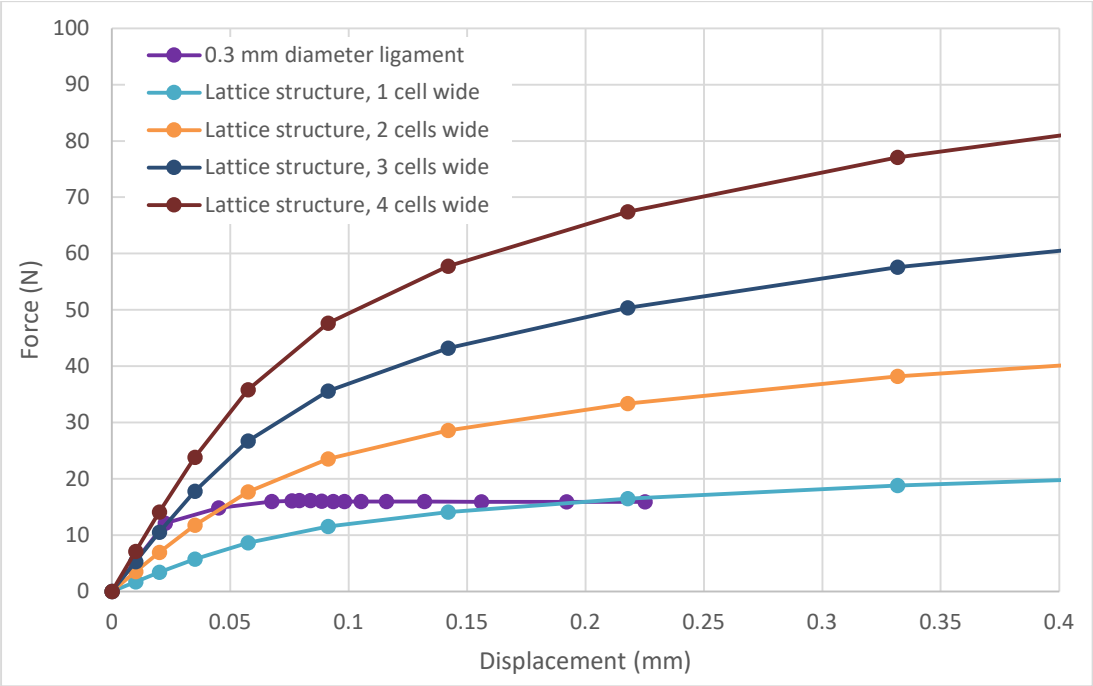

Figure 60 Force-displacement curves for the lattice structures of differing widths, compared with the single ligament data

The predictions obtained from the ligament and lattice models have been compared to the experimental data, see Figure 61. The initial stiffness of the experimental data is comparable with that predicted by the ligament model, but the measured force is much higher. The single unit cell model over predicts both the stiffness and the maximum force. The lattice model predicts loads approaching those measured, but at much larger displacements. This model also predicts a lower stiffness initially.

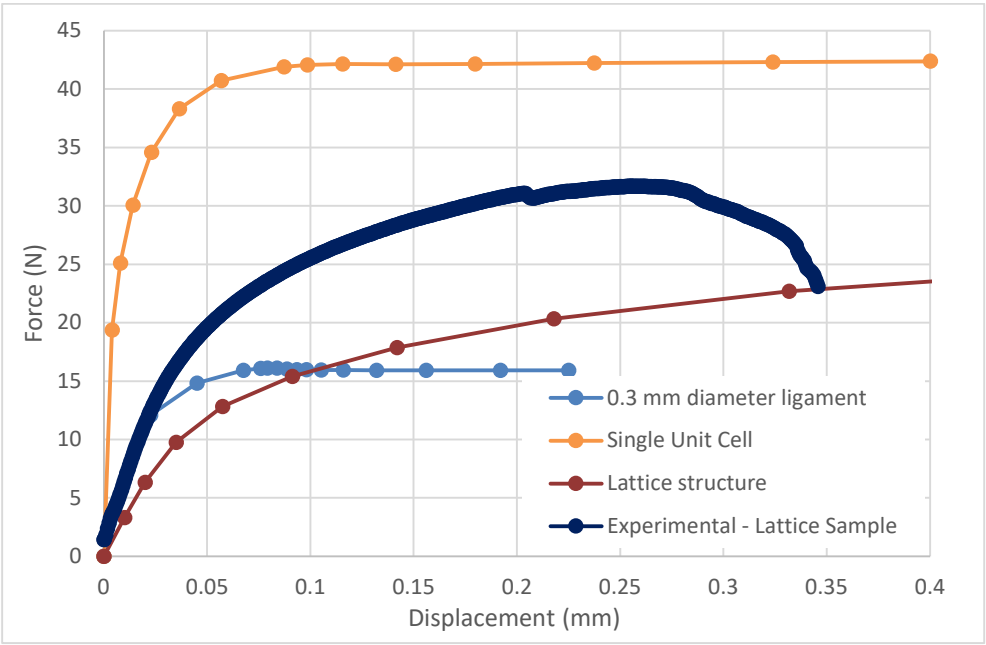

Figure 61 Comparison of the force-displacement plots obtained from the FE models with experimental data from the 0.3 mm diameter lattice sample

The high stiffness and predicted loads of the single cell geometry may be due to the model being over constrained. The free surfaces at the ends of the cell were constrained in the y and z directions, with a displacement applied to one end in the x direction. To investigate the effect of these constraints, a further model was created in which the free ends of the struts were allowed some movement in the y and z directions i.e., they could move closer to each other as the geometry is being 'stretched'. The predicted force-displacement from this model is compared to the previous data in Figure 62. By relaxing the constraints of the single unit cell model, the predicted curve has moved closer to the experimental data, showing a strong influence of applied boundary conditions to the predictions obtained.

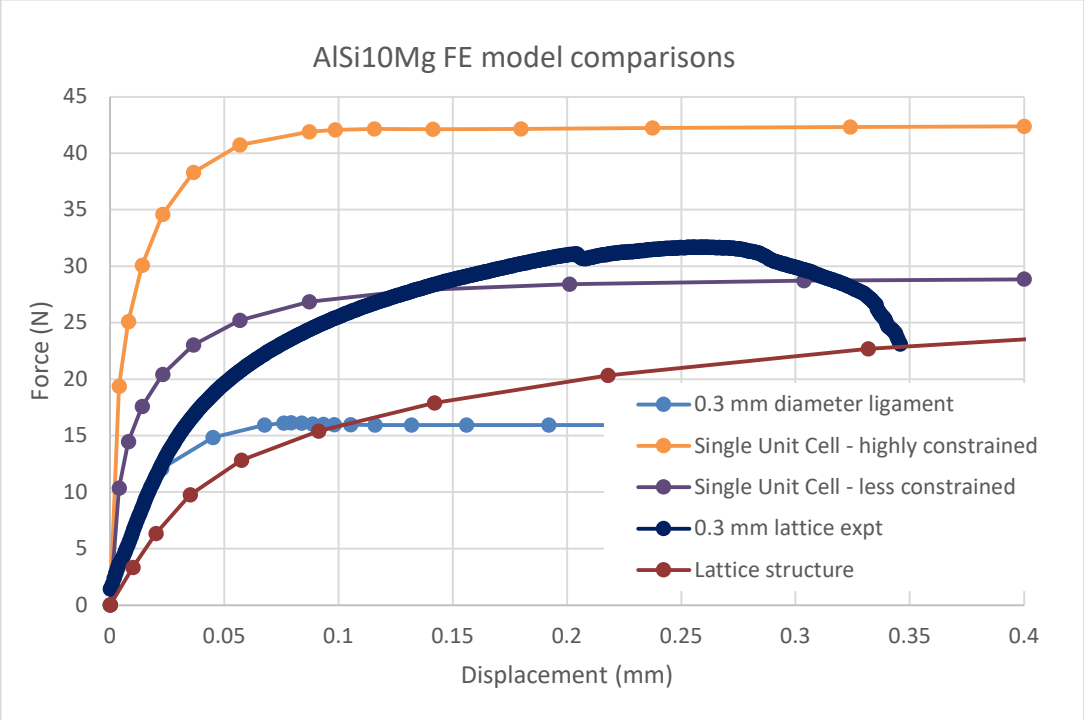

Figure 62 Comparison of the force-displacement plots obtained from the FE models, including the less constrained single unit cell, with experimental data

For the lattice geometry, nominal stress and global strain data have been calculated from the predicted force and displacements. Strains were also calculated from displacements taken over a set number of cells (either 1, 3 or 5 cells) within the central region of the sample, to compare to similar strain measurements obtained from the experimental data. Figure 40 shows an appreciable difference between the global strain and the localised strain measurements in the real sample. In the FE model, Figure 63, there is no obvious difference between the strains measured in different locations. This suggests that in the FE model uniform deformation is occurring throughout the sample.

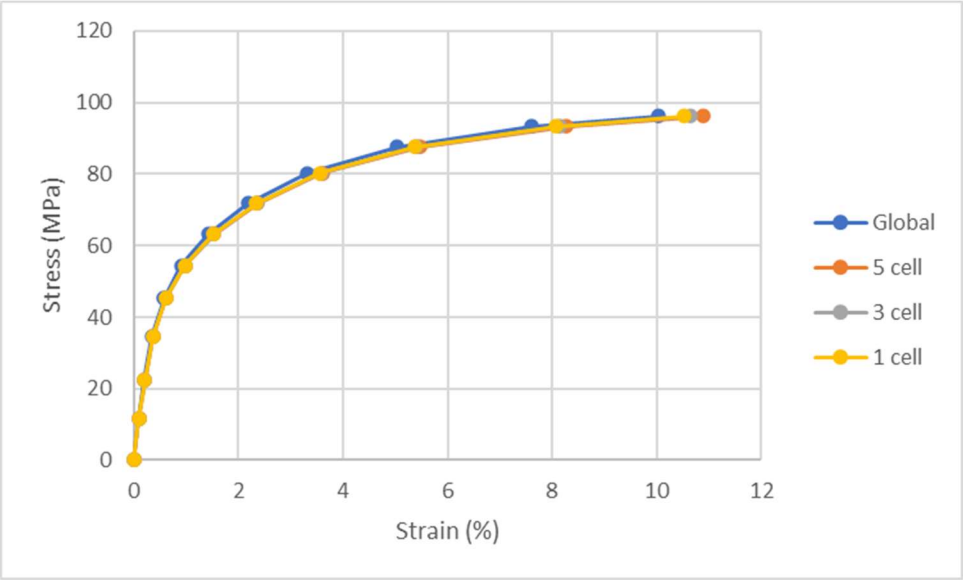

Figure 63 Stress – strain data predicted from the lattice geometry. Strains are obtained from the global displacement and also displacements across smaller numbers of cells in the centre of the sample.

When comparing this to the experimental stress-strain data it can be seen that the predicted curve is lower than the experimental curve i.e., there is a much larger strain predicted for any given stress, see Figure 64.

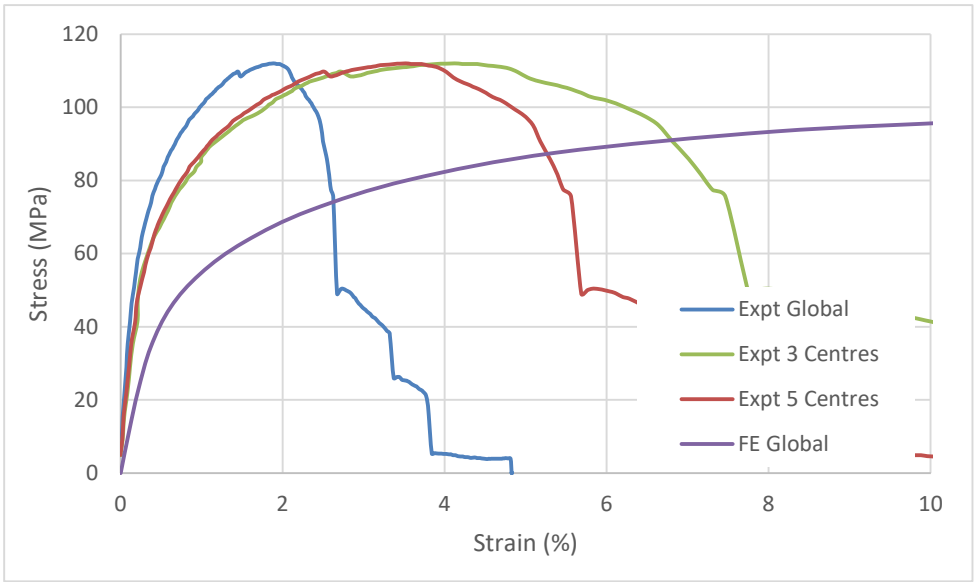

Figure 64 Comparison of FE lattice and experimental stress-strain data

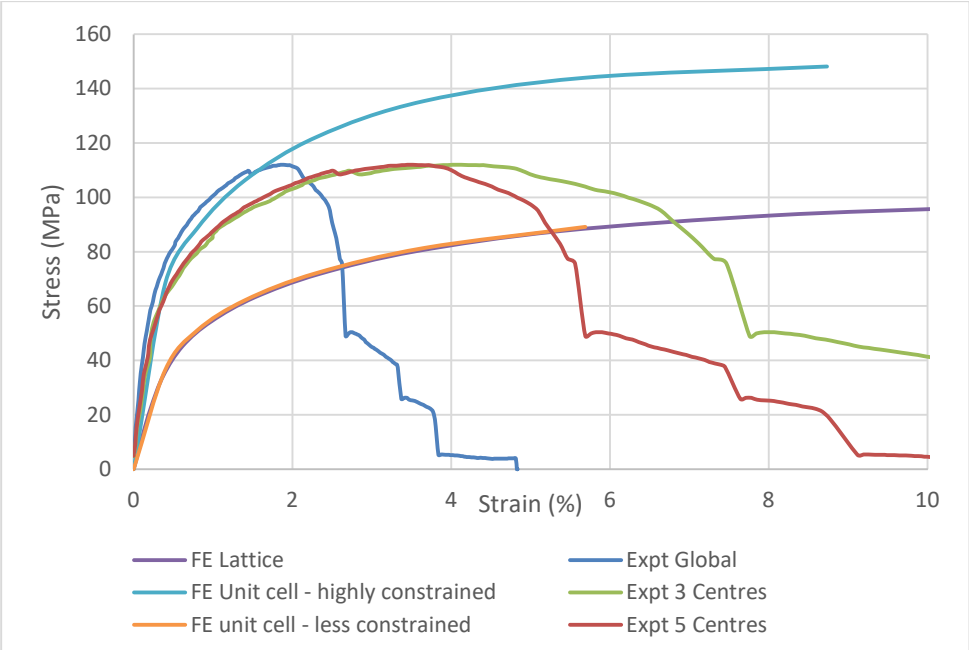

Figure 65 Comparison of FE lattice and single element models and experimental stress-strain data

Figure 65 shows the FE stress-strain predictions for the lattice sample and also the highly constrained and less constrained single unit cells. The highly constrained single unit cell predicts the correct initial stiffness but reaches much higher stresses than that measured experimentally. The predictions for the lattice sample and the less constrained unit cell are very similar to each other, but lower than the experimental data.

Possible reasons for the differences between the FE predictions and experimental results are discussed in Section 5.

5 DISCUSSION

Differences were observed in the mechanical response between single ligament test pieces tested on the universal test system and the Deben micro test system. Initially it was thought that the difference seen, i.e. the offset in the displacement data, could be due to microstructural effects in the material related to the rate of crosshead displacement. In particular there was a concern that the large-scale tests were initially conducted at too fast a rate to observe the same slope change seen in the Deben data. Duplicate tests were therefore conducted on the universal test system using the same displacement rate as that used with the Deben. The offset in displacement data and slope changes were not observed and so the test rate was not the cause of the differences in behaviour. One of benefits of using the micro test system is that the testing can be performed in the SEM and a high-resolution video of the test recorded. It was this recording of one of the Deben tests that has been subsequently used to perform digital image (DIC) correlation to help understand the deformation during the micro-tensile test of the single ligament.

Images were extracted from the test videos at a rate similar to the video frame rate. The images were then registered to correct for shifts in the field of view during the test [19,20]. Then DIC was performed using Augmented Lagrangian Digital Image Correlation (AL-DIC) [19,20]42 pixels with a 10% overlap. There was no iteration correction to remove any rigid body movement as the DIC being used here was purely meant to address any sample movement during the test. From the video capture there was no evidence of test piece slipping in the grips. Figure 66 show a series of image captures from the DIC video of the single ligament gauge length. A plot of the load and frame number (point) is shown in Figure 67.

In a purely tensile-loaded sample, you generally should not observe any displacement in the X direction (where this is perpendicular to the axial loading direction Y), especially if the sample is in the elastic region of the strain-stress curve, i.e., no plastic deformation or Poisson contraction. The sample was loaded in position control with a motor speed of 0.1 mm/min. Initially, the sample moved into the loading position with no exerted resistance, which would suggest that there was slack being taken up in the test frame, possibly though back lash. Displacement in X is seen at this part of grip movement with no load (Figure 67).

Once the sample ‘latched’ or secured, the initial load twisted the sample to align with the loading grip (one grip is moveable and the other is fixed in place to the frame). Here the displacement in X started to concentrate in the upper side of the sample (near the moving grip). As the test continued the displacement in Y also started to resemble a sample with uniform loading. The twisting or misalignment angle is determined as -2±1°. The areas highlighted in yellow, in Figure 68, are strange, as in this region the load and position remained almost fixed while the machine kept updating the number of recorded points. However, once load and strain continued, the overall displacement in Y increased incrementally with the load). At this point there remains an open question as to whether the misalignment is caused by the sample building process or the test rig.

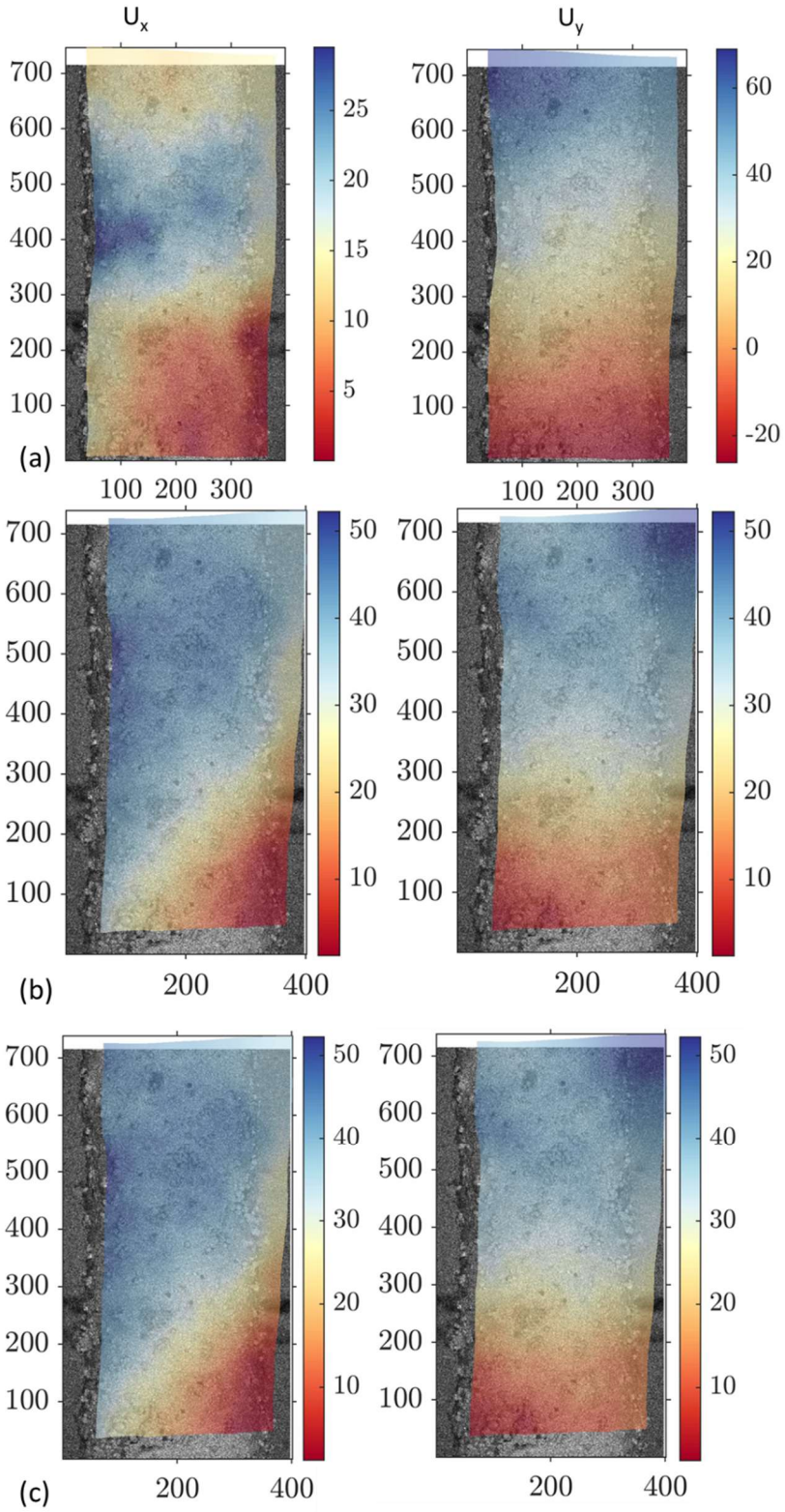

Figure 66 Images from the DIC analysis of the Deben micro tensile test at (a) point 15, (b) point 43 and (c) point 60 in Figure 67

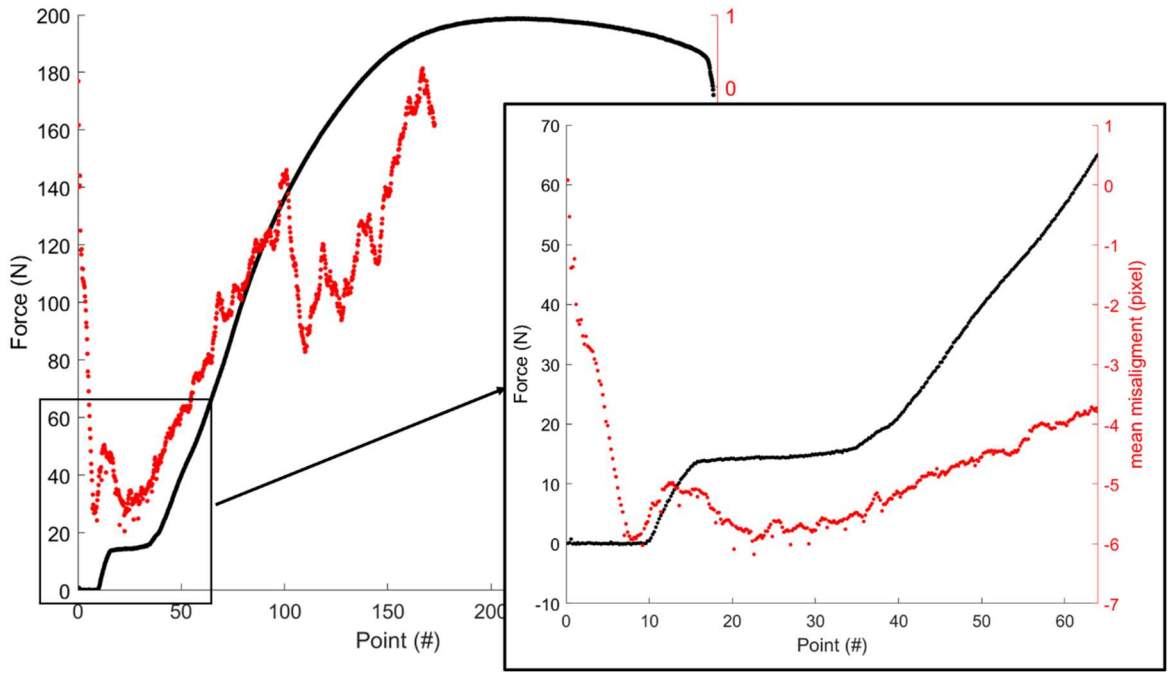

Figure 67 Force vs frame number (point) for the DIC analysis of the Deben micro test

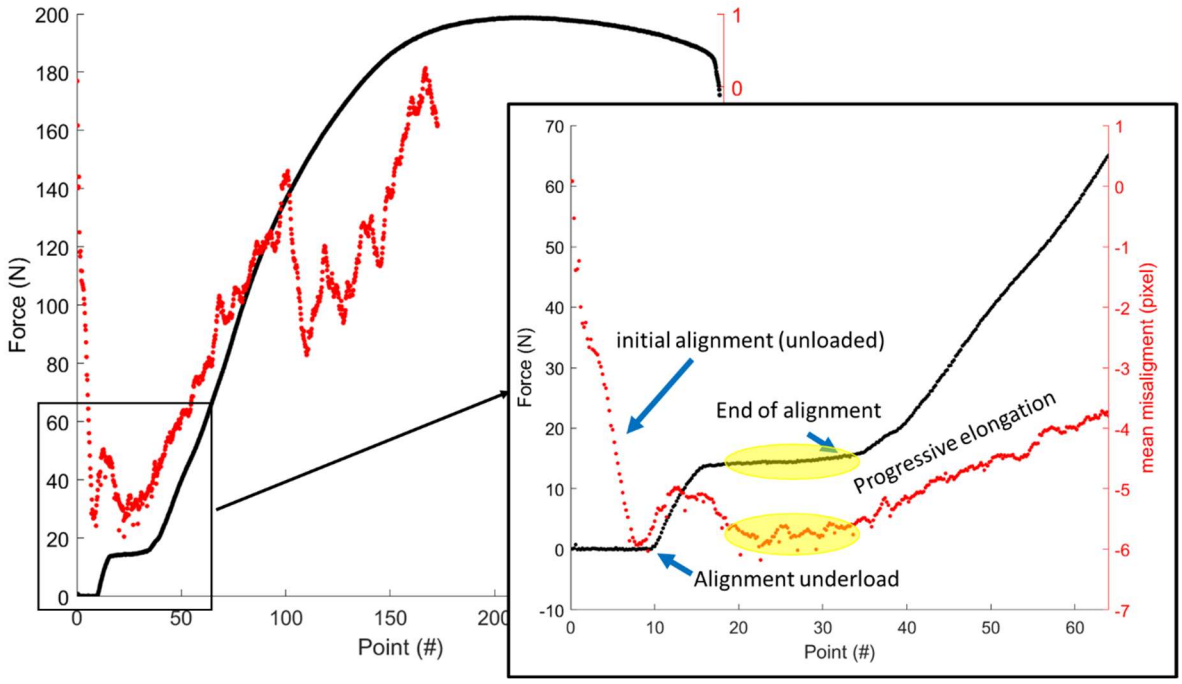

Figure 68 Force vs frame number (point) for the DIC analysis of the Deben micro test labelled to show the alignment features

Further DIC was conducted using a refined area with a subset of 20 pixels and a 50% overlap. Four iteration corrections were used to remove rigid body movement. The aim of the DIC was to identify strain build-up and localisation prior to the failure of the single ligament. Images from point 165 to 300 (Figure 67) were used for this DIC exercise. The rigid-body movement corrected DIC displacement image shows a uniform Y displacement and very faint X

displacement that start to localise in the top third of the sample. The localisation becomes more pronounced before the sample fracture, occurring at the site of localisation. The strain field where the fracture occurred is compressive on one side and tensile on the other side. The crack started from where tension was concentrated, shown in Figure 69.

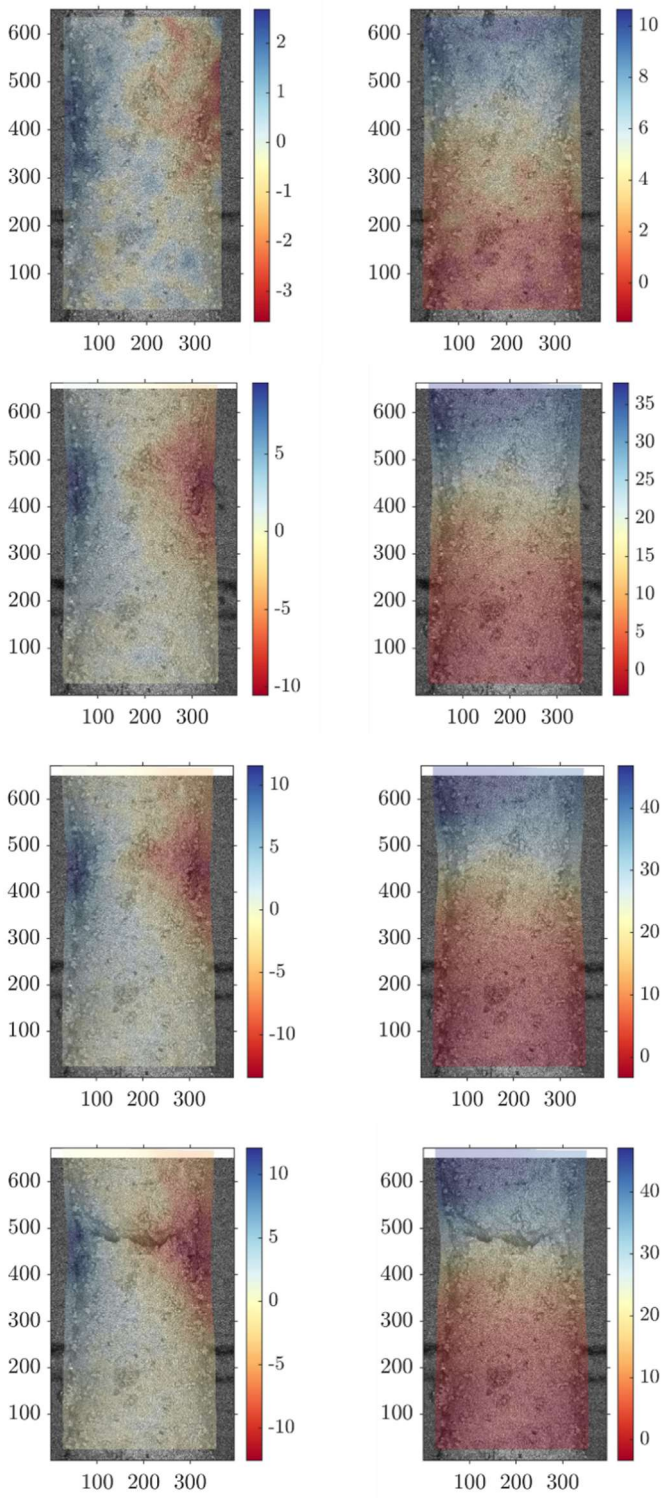

Figure 69 Images from the DIC analysis of the Deben micro tensile test, X displacement (left) and Y displacement (right)

There is a noticeable difference between the FE predicted data and the experimental results for the lattice structure.

In the FE analyses, there is very little difference between the global and localised strain predictions (Figure 63) suggesting that uniform deformation is occurring throughout the sample. This is clearly not the case in the experiments, where significant localised deformation is visible.

The close correlation between the single unit cell, highly constrained model predictions and the experimental data in Figure 65 might suggest that this FE model is representing the small region within the actual sample where the majority of the deformation is occurring. This region may be constrained by its neighbouring 'cells', leading to it being in a highly constrained state. The deviation of the experimental data from the FE data could be due to gradual failure of the material, which isn't included within the FE model.

There is a significant difference in the measured and predicted displacements. For the highly constrained single unit cell, the predicted displacements at any given load are much smaller than that measured experimentally (Figure 62), but when strains are calculated, they are much closer to those measured experimentally. Further investigation is required to understand the reasons for this.

The FE models an idealised geometry, where all struts are exactly 0.3 mm diameter, and each cell is completely uniform. It is clear from Figure 37, that this is not the case in the printed geometries where there is much more variability. Figure 38 shows the significant effect that a change in the strut diameter can have on the measured load-displacement response of the sample. The difference between the idealised geometry and the variability within the sample geometry may be a cause of some of the discrepancies between the experimental and FE predicted results.

6 CONCLUSIONS

The aim of this work was to develop and propose a test methodology to enable the tensile properties of lattices to be measured. The approach taken was to initially focus on the measurement to generate mechanical property data from a single lattice strut element and then use this data to generate an FEA model of the ligament. This model would then be used to generate a similar model for the lattice unit cell structure which could then be scaled up to simulate a lattice structure. It should be noted that the models being generated at this stage are oversimplifications and do not consider damage mechanisms or failure criterion.

- A specimen design was developed which enables the mechanical properties of single lattice strut elements to be measured in a universal test system and a in-situ micro test system.
- Tests conducted in the larger and stiffer universal test system and the micro test system exhibited some difference in the load-displacement response. This manifested itself in a low modulus initial portion of the load-displacement data. Analysis of this suggests it is caused by 'straightening' of the test system and the uptake of slack in the load train. This may be exacerbated by an 'straightening' or 'unwinding' of the lattice strut as load is applied.
- An FEA model of the single strut element has been produced with accurately simulates the stress-strain response of the ligament test piece.
- The single ligament test piece design has been extended to be used for testing lattice unit cells.

- Non-contact digital image correlation was successfully used to provide strain measurement on a global and discrete scale for the single strut and lattice unit cells for different test systems.
- The FEA model was extended to be able to model the stress-strain response of the lattice unit cell. At this point the FEA model does not predict failure or damage accumulation.
- The measurement approach demonstrated in the report has been successfully used to measure the mechanical properties of lattice unit cells made with 0.3 mm and 0.25 mm struts.

Future work will address further scaling up of the lattice and issues associated with the placement of nodes and sectioning points in the lattice test piece and the influence these have on the mechanical property response of the test piece.

7 REFERENCES

1. Maconachie, T. *et al.* SLM lattice structures: Properties, performance, applications and challenges. *Mater Design* 183, 108137 (2019).

2. Maskery, I. *et al.* A mechanical property evaluation of graded density Al-Si10-Mg lattice structures manufactured by selective laser melting. *Mater Sci Eng* 670, 264–274 (2016).

3. Choy, S. Y., Sun, C.-N., Leong, K. F. & Wei, J. Compressive properties of Ti-6Al-4V lattice structures fabricated by selective laser melting: Design, orientation and density. *Addit Manuf* 16, 213–224 (2017).

4. Tancogne-Dejean, T., Spierings, A. B. & Mohr, D. Additively-manufactured metallic micro-lattice materials for high specific energy absorption under static and dynamic loading. *Acta Mater* 116, 14–28 (2016).

5. Alsalla, H., Hao, L. & Smith, C. Fracture toughness and tensile strength of 316L stainless steel cellular lattice structures manufactured using the selective laser melting technique. *Mater Sci Eng* 669, 1–6 (2016).

6. Qiu, C. *et al.* Influence of processing conditions on strut structure and compressive properties of cellular lattice structures fabricated by selective laser melting. *Mater Sci Eng* 628, 188–197 (2015).

7. Kempen, K., Thijs, L., Humbeeck, J. V. & Kruth, J.-P. Mechanical Properties of AlSi10Mg Produced by Selective Laser Melting. *Physcs Proc* 39, 439–446 (2012).

8. Kempen, K., Thijs, L., Yasa, E. & Badrossamay, M. Process Optimization and Microstructural Analysis for Selective Laser Melting of AlSi10Mg. in *International Solid Freeform Fabrication Symposium* (2011).

9. Brandl, E., Heckenberger, U., Holzinger, V. & Buchbinder, D. Additive manufactured AlSi10Mg samples using Selective Laser Melting (SLM): Microstructure, high cycle fatigue, and fracture behavior. *Mater Design* 34, 159–169 (2012).

10. Gibson, L. J. & Ashby, M. F. Cellular Solids. 93–174 (1997) doi:10.1017/cbo9781139878326.006.

11. Leary, M. *et al.* Selective laser melting (SLM) of AlSi12Mg lattice structures. *Mater Design* 98, 344–357 (2016).

12. Gavazzoni, M., Pisati, M., Beretta, S. & Foletti, S. Multiaxial static strength of a 3D printed metallic lattice structure exhibiting brittle behaviour. *Fatigue Fract Eng M* 44, 3499–3516 (2021).

13. Park, S.-Y., Kim, K.-S., AlMangour, B., Grzesiak, D. & Lee, K.-A. Effect of unit cell topology on the tensile loading responses of additive manufactured CoCrMo triply periodic minimal surface sheet lattices. *Mater Design* 206, 109778 (2021).

14. Scalet, G., Biffi, C., Fiocchi, J., Tuissi, A. & Auricchio, F. Additively manufactured Ti6Al4V lattice structures: mechanical characterization and numerical investigation. *Iop Conf Ser Mater Sci Eng* 1038, 012057 (2021).

15. Wang, X. *et al.* Evaluating Lattice Mechanical Properties for Lightweight Heat-Resistant Load-Bearing Structure Design. *Materials* 13, 4786 (2020).

16. Kandil, F. A. *A PROCEDURE FOR THE MEASUREMENT OF MACHINE ALIGNMENT IN AXIAL TESTING Report No. 42 ISSN 1016-2186*.

17. Kandil, F. A. *VAMAS Technical Working Area 13 on Low Cycle Fatigue: An Overview of its Work and Achievements*.

18. L, Remy, F, Rezai.-Aria., R, Danzer. & W, Hoffelner. Low Cycle Fatigue. 1115-1115–18 (1988) doi:10.1520/stp24542s.

19. Koko, A., Earp, P., Wigger, T., Tong, J. & Marrow, T. J. J-integral analysis: An EDXD and DIC comparative study for a fatigue crack. *Int J Fatigue* 134, 105474 (2020).

20. Yang, J. & Bhattacharya, K. Augmented Lagrangian Digital Image Correlation. *Exp Mech* 59, 187–205 (2019).